Chapter 15
Clinical Results with Ultrasound Computed Tomography of the Breast

Michael André, James Wiskin and David Borup

Abstract Although the science and engineering of ultrasound computed tomography (USCT) has been explored for over four decades, there have been relatively few instances of a system being developed and applied to patients. Nonetheless, there have been notable results from the clinical setting, especially recently, that illustrate how a successful USCT scanner may provide significant advances to women's health. For practical anatomical reasons, this work has almost exclusively addressed imaging of the female breast. Other quantitative ultrasound techniques have been applied to characterizing the female breast, including quantitative backscatter analysis, shear wave speed, computer-aided diagnosis, etc., but USCT is the focus of this chapter. We highlight the evolution of scanner design and image reconstruction by presenting key results from patient measurements by the major researchers in the field. There has been steady progress in electronics, parallel processors, reconstruction algorithms, understanding of the physical properties of breast tissue and a resurgence of interest in the medical community for dedicated breast ultrasound systems. It is understood today that USCT may be able to contribute in many aspects of the medical management of breast disease including detection, diagnosis and treatment of breast cancer.

M. André (✉)
Radiology, Physics & Engineering Division 114, VA Healthcare/University of California, San Diego, 3350 La Jolla Village Drive, San Diego, CA 92161, USA
e-mail: mandre@ucsd.edu

J. Wiskin · D. Borup
CVUS, LLC, 3216 Highland Dr.Suite 100, Salt Lake City, UT 84106, USA
e-mail: jwiskin.cvus@gmail.com

D. Borup
e-mail: dborup@comcast.net

J. Mamou and M. L. Oelze (eds.), *Quantitative Ultrasound in Soft Tissues*, DOI: 10.1007/978-94-007-6952-6_15,

15.1 The Medical Problem

The American Cancer Society estimated in 2011 that the lifetime risk for breast cancer is 12.15 % or 1 in 8 and the death rate is exceeded only by lung cancer in women (American Cancer Society 2011). In addition, about 1 % of all breast cancers occur in men. The National Cancer Institute estimated that in 2008 approximately 2.6 million women with a history of breast cancer were alive in the U.S. (Howlader et al. 2011). Breast cancer originates in the glandular tissue, called lobules, and in the ducts that connect them to the nipple. The remainder of the breast is connective tissue and fat, the relative composition of which may change with age and other factors. There are many known relative risk factors for breast cancer but the dominant one is age; incidence and death rates increase with age such that 97 % of breast cancer deaths occur in women 40 years of age and older. The majority of masses that occur in the breast are benign, not threatening and many may be identified with confidence on mammograms or sonograms. However, a significant number of masses are either not seen on screening mammography or the findings are not conclusive without further workup. Early detection of breast cancer when the mass is small is very important to survival rate; 5 year survival for women with cancer $\geq$20 mm is 80 % compared to 98 % for masses 10 mm (American Cancer Society 2011).

15.1.1 Current Breast Cancer Imaging

Mammography is the primary screening tool for breast cancer together with physical examination, while breast sonography is the principal adjunctive imaging modality. As a general rule, a screening test is desired to have very high sensitivity to disease with few or no false negative results. This often results in lower specificity, leading to higher false positives that require further clinical evaluation. A suspected finding in screening may advance the patient to a diagnostic examination. In this case the patient has additional specialized mammograms or very commonly, a diagnostic breast sonogram is obtained possibly of only a portion of one breast in the region where the finding is located. The handheld transducer used in the diagnostic sonogram is also well suited to provide guidance for performing a needle aspiration or core biopsy when a mass is identified that is suspicious for cancer. In some instances the patient may undergo a magnetic resonance imaging (MRI) breast examination that entails injection of a vascular contrast enhancing material incorporating gadolinium, although it is impractical for use in general screening. MRI has high sensitivity and is considered to provide the most accurate depiction of the margins of a malignant mass so it is often used for surgical planning and monitoring response to therapy. As a screening test applied to many millions of patients, mammography is relatively inexpensive, sonography costs approximately 2–3 times more, while breast MRI is up to 10 times more expensive

than mammography. Representative mammograms, sonograms and MRI images are compared later in the chapter.

15.1.2 Breast Sonography

Conventional sonography systems produce images of reflected and backscattered ultrasound energy, or relative "echogenicity," that occur at interfaces between the different breast tissues. Image formation assumes straight-line propagation, 180° backscatter and constant sound speed, usually 1,540 m/s, all of which are known to be incorrect. Breast ultrasound is recognized to be a difficult exam to perform and interpret while image quality is known to be dependent on the skill of the operator as well as technical features of the scanner. A major strength of breast ultrasound and its most common clinical use is differentiation of cystic and solid lesions with nearly 100 % accuracy (Stavros et al. 1995, 2005; Hong et al. 2005; Brogoch et al. 2010). Nonetheless, numerous studies of conventional breast ultrasound show substantial variance in diagnostic accuracy due to variability in radiologists' skill levels (Baker et al. 1999) and technical features of the scanner (Berg et al. 2006).

Work to improve the accuracy of diagnostic breast ultrasound led to the development of a well-defined rule-based system for mass assessment based on parameters describing the ultrasound appearance of breast lesions. Sonographic features of a mass are described in accordance with the ACR Breast Imaging Reporting and Data System® (BI-RADS®) (Mendelson et al. 2003). The BI-RADS sonographic categories include size, shape, margin, relative echogenicity, lesion boundary, orientation to the skin, posterior features (shadowing or enhancement due to different attenuation), vascularity, and surrounding tissue. A final numerical assessment is reported on an increasing scale of risk for cancer, 1–5, as well as 0 where more information is needed and 6 where the finding is a known cancer. Precise application of the BI-RADS approach was shown to be helpful in differentiating benign versus malignant solid masses, particularly when performed by experts, although there is variability between readers (Brogoch et al. 2010; Baker et al. 1999; Berg et al. 2006; Mendelson et al. 2003; Kwak et al. 2006; Kolb et al. 2002). Mass characterization with ultrasonography is highly dependent on technical factors and settings of the scanner. Example images of three masses are shown in Fig. 15.1. Posterior "enhancement" is evident for the fluid-filled simple cysts (Fig. 15.1a), while posterior "shadowing" is seen for the malignant mass (Fig. 15.1c). These effects are artifacts due to application of time-gain compensation in regions where attenuation and reflection losses are not uniform with depth.

The American College of Radiology (ACR) published breast ultrasound practice guidelines to establish standards for indications of use, qualifications and responsibilities of the practitioner, examination procedures, quality control, minimum equipment specifications and more (ACR 2011). Following these standards breast ultrasound should be performed with linear array transducers of 10 MHz or more and with variable focal zones. In order to obtain the needed high resolution,

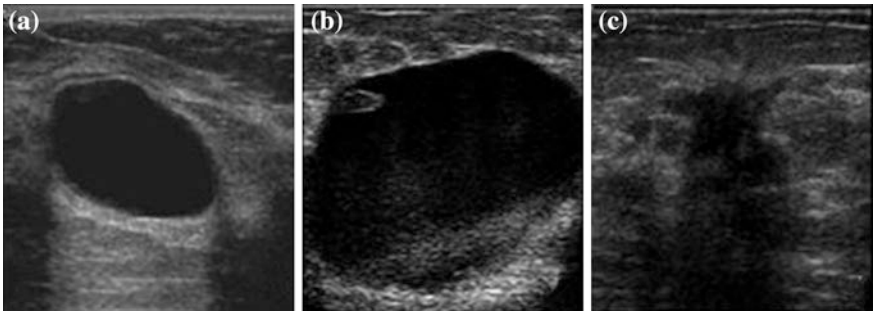

Fig. 15.1 Three sonograms of breast masses where the transducer is applied to the skin at the top of the images. **a** Simple cystic mass with distinct margins. **b** Large complex cystic mass with internal echoes and debris. **c** Spiculated solid malignant mass. The field of view and range for these images is 4 cm

the field of view and range in sonography is small, which greatly complicates interpretation, localization of masses and comparison to prior exams. The sonogram is performed with the patient supine in order to minimize the thickness of the breast in accommodation of the high attenuation and small field of view at high frequency. It can be difficult to precisely describe or record the location of a finding in the breast since the tissue can be mobile. This complicates serial monitoring of a mass over time and in some cases it is difficult to find a mass at the time of biopsy that was seen in an earlier visit. BI-RADS uses a "face-of-the-clock" scheme for sonography with the nipple at the center and the caudal direction at 12:00, but of course the breast is three dimensional. These same issues may complicate other quantitative enhancements to breast sonography including shear wave speed (Berg et al. 2012) or elastography methods, and computer-aided diagnosis (Andre et al. 2011).

15.1.3 Whole-Breast Ultrasound Imaging

Even with the best imaging methods available today, up to 80 % of breast biopsies performed turn out to be benign (Silverstein et al. 2005; Kolb et al. 2002; Stavros 2004). Combined mammography and targeted breast ultrasound is still the most effective approach for breast cancer screening in women at normal risk (Silverstein et al. 2005; Stavros 2004). Adding a single screening ultrasound to mammography yields an additional 1.1–7.2 detected cancers per 1000 in high risk women, but at an increase in false positive findings (Silverstein et al. 2005; Shetty et al. 2003).

Despite the potential benefits, sonography is not usually employed for screening due to several factors including procedural complexity, additional skill and training required, a long procedure time, the requirement that a radiologist perform it, the large number of images that need to be reviewed and cost. Nonetheless sonography is being more widely employed particularly for younger women for whom mammography may not be recommended and women with dense breasts

where mammography is less sensitive. For women with particular risk factors, breast sonography may be indicated as a secondary screening modality.

The American College of Radiology Imaging Network (ACRIN) Trial 6666 examined the role of whole-breast ultrasound (WBU) screening with conventional scanners at multiple centers for several thousand patients with moderate risk factors for cancer (Berg et al. 2008). In this procedure, a high frequency hand-held transducer is slowly scanned across the entire breast in an overlapping raster fashion while the patient lies supine. The ACRIN protocol for scanning both breasts took 20–40 min and required that the procedure be performed and interpreted by a radiologist with special proficiency. A semi-automated system to facilitate this procedure was developed by Sonocine (Reno, NV) that has received approval from the U.S. Food and Drug Administration (Kelly et al. 2010). Any suitable breast ultrasound transducer system is attached to a mechanically-driven arm manipulated by the sonographer while the system records the position, angle and tip of the linear array. Overlapping passes are made of the breast while the sequence of up to 1,000 or more closely-spaced images of the breast is recorded. The radiologist reviews the images while they are displayed in rapid sequence, at a rate of a few per second, in two-dimensional (2D) mode as a cine loop. ACRIN 6666 and studies published by Sonocine show that there is a significant increase in the number of cancers detected by WBU over mammography alone.

A particularly noteworthy substudy of ACRIN 6666 examined the effect of supplementing annual mammography screening with annual ultrasound over a three-year period in 2809 women at elevated risk due to radiographically dense breast tissue and at least one additional risk factor such as personal and/or family history of breast cancer (Berg et al. 2012). Adding ultrasound to mammography each year significantly increased the chance of finding invasive cancer before it spread to the lymph nodes. Of the 111 breast cancer diagnoses in this group, mammography failed to see about half of the cancers present in women with dense breasts although it did detect 33 cancers not seen on sonography. 32 cancers were seen only by ultrasound of which 94 % were node-negative invasive. 26 were detected on both mammograms and sonograms, while 9 were seen only by a single MRI exam performed after three years of mammography and sonography. 11 were not detected by any imaging screen during this period. Adding annual sonography and a single MRI increased false positives by 5 % but they provided a significant detection benefit for these women. Neither ultrasound or MRI are recommended as a replacement for mammography, but it is important to emphasize that the vast majority of additional cancers detected by supplemental sonography were early-stage invasive cancers that had not spread to the lymph nodes. If a patient has an MRI the ultrasound is probably not needed and possibly vice versa for reasons of practicality.

In the U.S. 14 states have passed legislation requiring breast imaging centers to inform patients if they have mammographically dense breast tissue. The legislation is based on the proposition that breast density is a strong risk factor for breast cancer. When the breast is comprised of less fat and more glandular tissue it represents a challenge for mammography to detect masses. Categorizing breast

tissue is a component of the mammographic BI-RADS protocol but it is highly qualitative and variably applied. WBU has been shown to precisely differentiate between fat and fibroglandular tissues while in addition USCT can provide quantitative volumetric measurements of the tissues.

15.1.4 Opportunity for Ultrasound Computed Tomography

The discussion in the two previous sections describes many of the benefits and limitations of conventional breast sonography. It also illustrates there is an opportunity for new technology to play an important clinical role in breast cancer detection, diagnosis and management. Whole breast USCT using transmission and/or reflection techniques has been proposed for many years as a means to address the shortcomings but also to provide entirely new ways to assess and characterize masses and other findings in the breast.

The promise of USCT is based on several key attributes including:

- ability to provide global views of both breasts in a standard frame of reference for detailed contralateral and serial comparisons
- operator independence
- uniform high resolution independent of range and location
- minimal refraction, spatial distortion or multiple scattering effects
- no speckle
- quantitative tissue properties of sound speed, attenuation and scatter
- ability to precisely locate findings to facilitate follow-up exams
- volumetric images to aid monitoring changes due to therapy
- anatomic breast positioning with no compression or distortion
- fast scans of the entire breast
- characterization of masses based on quantitative properties and accurate morphometry
- accurately measures relative volumes of fat and glandular tissues
- significant improvements in both high speed data multi-channel acquisition systems and powerful multi-processor computing.

The experimental basis for this promising opportunity is summarized in the next section in which some of the notable clinical studies of USCT are reviewed.

15.2 Breast Ultrasound Computed Tomography

Research in a number of laboratories in the 1970s and 1980s showed potential for USCT to provide accurate spatial registration, high spatial and contrast resolution, few artifacts and quantitative tissue measurements, particularly of sound speed,

attenuation and morphometry. However, with over four decades of research there have been relatively few instances of practical systems being developed and applied to patients. Instead the majority of the research work addressed theoretical and computational developments. These early prototype scanners were mostly very slow, with few data channels, sparse spatial sampling and long reconstruction times limited by available technology. The U.S. medical community largely concluded this work was premature or unnecessary given the success of high-quality, fast, automated array technology that had multiple medical uses beyond breast imaging (Carson and Fenster 2009). The research also illustrated USCT is a highly complex, inherently non-linear problem that probably requires consideration of the three-dimensional (3D) nature of sound propagation. With steady scientific progress and new technology there is a revival of effort in this field and the latest results are impressive. The developments described earlier that are expanding the role for ultrasound in breast imaging have also enhanced the opportunity for USCT to emerge from the laboratory.

Four approaches to USCT will be considered in three categories described in Chap. 1: (a) ray-based backprojection, (b) diffraction tomography with an annular array and (c) full-wave inverse-scatter tomography (IST) with reflection tomography (RT). With the exception of recent work in IST, all of the approaches used 2D linear approximations to obtain sequential coronal planes through the breast. Two USCT systems developed by the authors are explored in some detail; one early diffraction tomography unit and the current full-wave inverse-scattering tomography system.

15.3 Ray-Based Backprojection Tomography

The earliest attempts at USCT used transmission time of flight (TOF) and amplitude measurements along straight rays combined with CT reconstruction methods analogous to x-ray CT. Greenleaf et al. (1974, 1975, 1978) were probably the first to describe results with ultrasound transmission tomography, while Glover and Sharp (1977); Glover (1977) may have been the first to show results in patients. Carson et al. (1981) was also actively imaging patients with a similar system. Others worked with B-mode methods to produce reflection tomograms (Carson et al. 1981; Mueller et al. 1979; Hiller and Ermert 1980).

In 1981, Greenleaf and Bahn (1981) published clinical results from approximately 150 patients, 30 of whom had biopsy-confirmed breast cancer. The scanner employed 5 MHz single-element transmit-receive pairs, initially one pair and later additional stacked in a vertical line that could acquire multiple planes of 2D data with each rotation (Fig. 15.2). 2.4×10^4 transmission rays were acquired to produce a 118×118 image matrix using filtered backprojection, examples of which are shown in Fig. 15.3 for an adenocarcinoma. The patient lay supine with one breast suspended in a water bath while the transducer pairs rotated 360°.

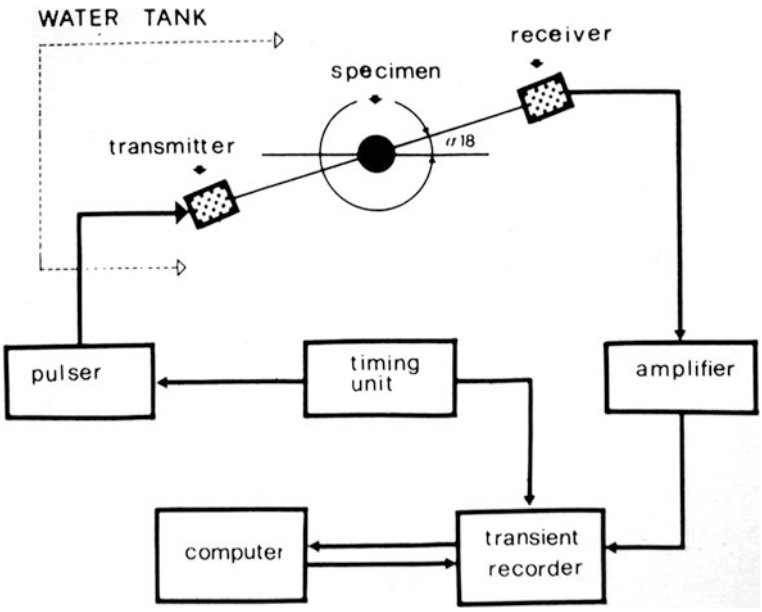

Fig. 15.2 Rotating transmit-receive pair of transducers obtained time-of-flight and signal amplitude data for reconstruction by filtered backprojection. Adapted from Greenleaf et al. (1978)

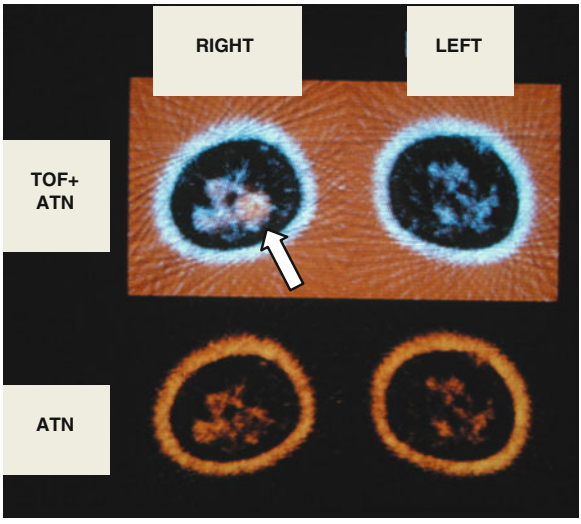

Fig. 15.3 Sound speed (*TOF*) is displayed in *blue* and attenuation (*ATN*) in *red* for *right* and *left* breast. The two are superimposed in the *top row* to emphasize the location of the mass (*arrow*). Adapted from Greenleaf et al. (1978)

The researchers carefully analyzed the calculated ultrasonic properties and pathological findings of both normal breast tissues and masses for patients who later had mastectomy. All solid lesions were found to have relatively higher sound speed in association with varied patterns of attenuation. Figure 15.4 demonstrates

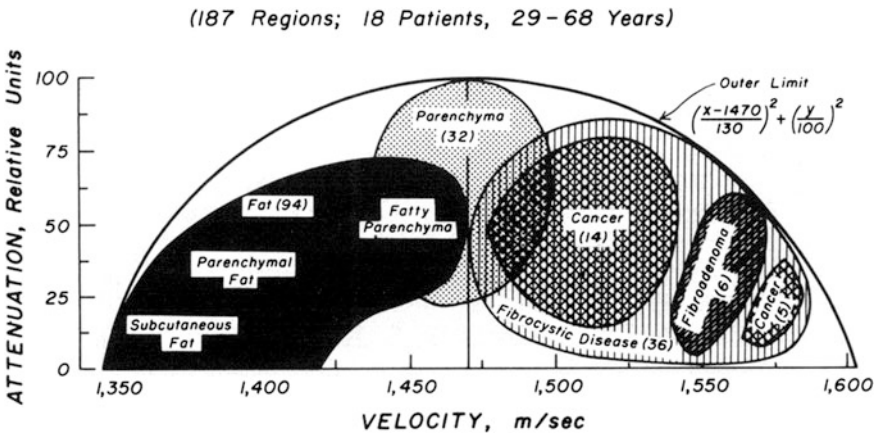

Fig. 15.4 Relationship between sound speed and attenuation for normal tissues and masses. Adapted from Greenleaf and Bahn (1981)

the results of their analysis showing the relationship between sound speed (velocity) and attenuation. Overall a broad distribution of values was found with overlap of benign and malignant masses using only these two features. Several different classification schemes were tested with resulting specificity of 80–90 % (Greenleaf and Bahn 1981).

Carson et al., developed a system employing opposing 3.5 MHz transducers in a 20 °C water tank that used a translate-rotate motion around the breast to acquire 90 views or linear profiles with filtered backprojection reconstruction (Carson et al. 1981). Both transmission tomograms and compounded pulse-echo images were produced, the latter formed on an analog scan converter. Figure 15.5 shows images for a 41 year-old patient with a 1.8 cm infiltrating ductal carcinoma in the

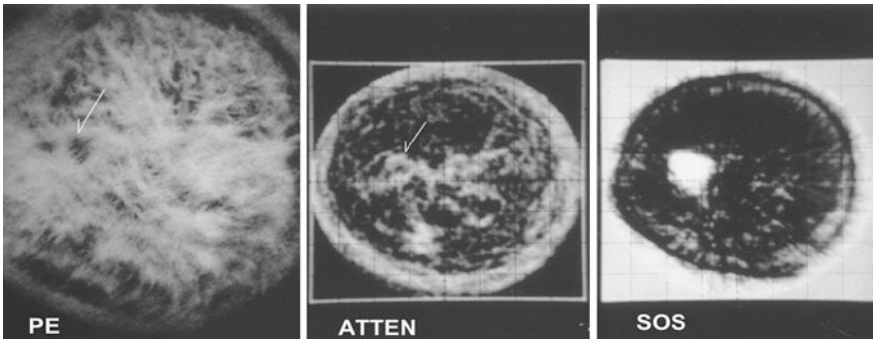

Fig. 15.5 Coronal images of compounded pulse echo (*PE*), attenuation (*ATTEN*) and speed of sound (*SOS*) were obtained 9 cm from the nipple in a breast with infiltrating ductal carcinoma. The mass is indicated by the arrows and readily seen in the SOS image as a bright white irregular shape at 9:00 (Carson et al. personal communication)

9:00 location (arrows). Image features include high sound speed (1,531 m/s) surrounded by low speed fat (1,445 m/s). The mass is less echogenic than the surrounding tissue in the pulse-echo image and it appears to have attenuating borders (ATTEN). Not surprisingly, detection of malignancy was found to be more difficult with smaller masses and in younger patients with denser breasts.

Analysis similar to that of Fig. 15.4 was performed of the ultrasonic properties of 40 lesions. The speed of sound and attenuation relative to the surrounding mammary tissue are plotted in Fig. 15.6 for normal tissues, unclassified benigns and fibroadenomas (all solid dots), for cysts (open circles) and for cancers (5). In this three-group analysis it is apparent that four benign lesions including one cyst are classified with cancers. The overall sensitivity and specificity are quite good, both greater than 90 % (Carson et al. 1983, Scherzinger et al. 1989).

A recent clinical prototype imaging system was developed that employs a ray-based tomographic reconstruction but utilizes a stationary circular array without rotation (Duric et al. 2005, 2007). It bears some resemblance to the design of a previous diffraction tomography system (André et al. 1997) described in the next section but has numerous improvements. The array consists of 256 elements operating at 1.5 MHz, equally spaced on a diameter of 20 cm that is translated vertically to acquire successive planes. There are 256 data acquisition channels sampling at 6.25 MHz. This design affords very fast acquisition for a single slice ($\sim$100 ms) with about 45 slices acquired per breast for a total exam time of 5 min. Transmitted and reflected data are acquired to produce a reflection tomogram and

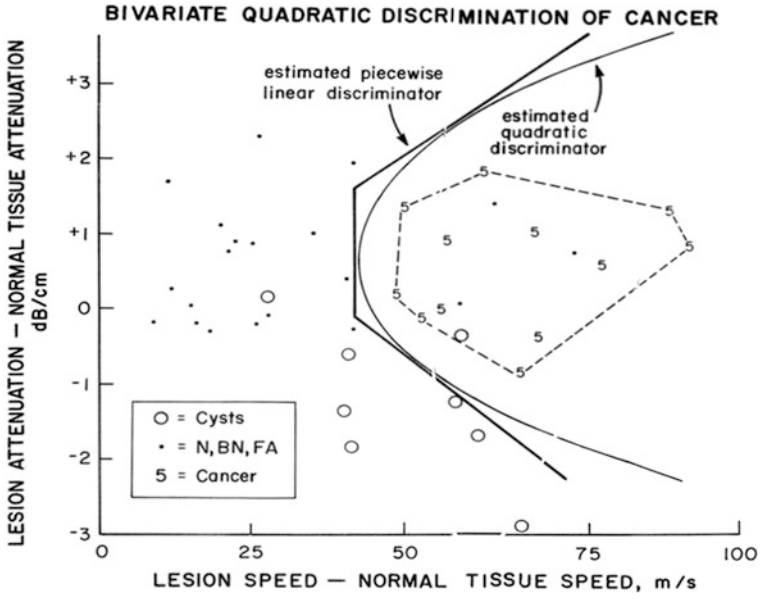

Fig. 15.6 Measured ultrasound characteristics of tissues and lesions. Adapted from Carson et al. (1983)

coincident images of sound speed and attenuation. Performance in phantoms met expectations with in-plane resolution for the transmission images of 4 mm, 0.5 mm in the reflection mode ($\sim\lambda/2$) and with effective slice thickness of 12 mm. Spatial resolution is limited by the size and spacing of the elements plus the large slice thickness (Fig. 15.7).

Sample images are shown in Fig. 15.8 from a patient whose subsequent biopsy proved invasive ductal carcinoma. The mass shows higher sound speed and attenuation compared to surrounding tissues (whiter) with apparent architectural distortion evident in the higher resolution reflection image. In a small patient study six features were found to be associated with malignancy: ratio of width to height $<$1.4, irregular shape, irregular margins, architectural distortion, elevated sound speed of 50–150 m/s relative to fat and elevated attenuation of 0.5 dB/cm relative to fat at 1.5 MHz (Duric et al. 2006). In addition to characterizing masses, this prototype scanner has shown potential value of the sound speed images for monitoring response to neoadjuvant chemotherapy. Inability to account for out-of-plane scattering and refraction limits accuracy of the attenuation measurements. The group has designed a production level scanner with apparently 2,048 elements that will be capable of much higher resolution and better in-plane focusing.

Although the results were very encouraging, these studies showed that the breast contains considerable complexity with as much as $\pm$8 % variation in sound speed and 4 dB/cm/MHz attenuation. Given the long path length, variations in refractive index are not negligible nor are refraction and multiple scattering. Consequently, the straight-ray image inversion methods are likely to prove inadequate for most clinical use.

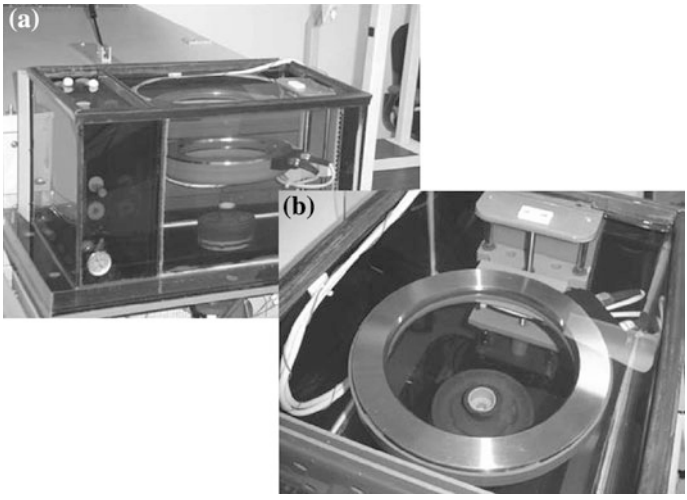

Fig. 15.7 Ring transducer array in the water tank that is positioned below the patient table for scanning. From Duric et al. (2005)

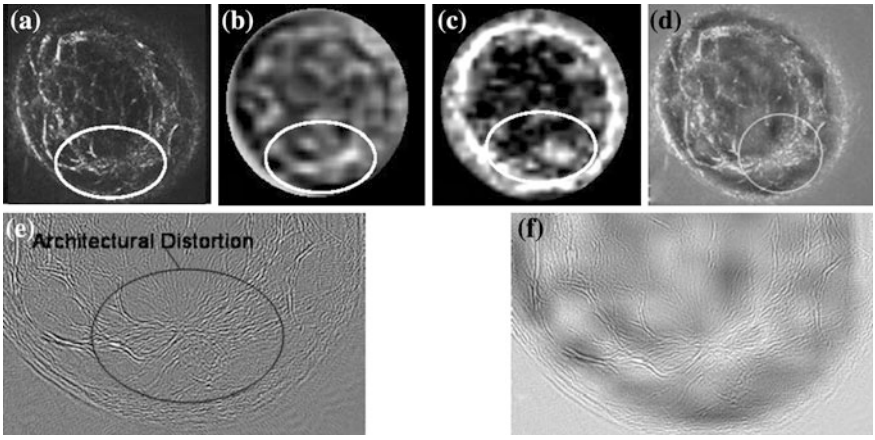

Fig. 15.8 Images of a 10 mm invasive ductal carcinoma located inside the oval. **a** Reflection image. **b** Sound speed. **c** Attenuation. **d** Sound speed fused with reflection. **e** Close up of edge enhanced reflection image showing distortion. **f** Close up of (**d**). From Duric et al. (2006)

15.4 Diffraction Tomography

In ultrasound computed tomography, the wavelength of sound in tissue is on the order of 1 mm and the effects of diffraction are not negligible. In general, due to limitations of instrumentation and algorithms, the second stage in development of ultrasound transmission imaging was to solve wave equations using two-dimensional linearization techniques rather than geometrical ray models for reconstruction. In its simpler forms this approach usually fails for breasts because it is based on first-order perturbation approximations (Born or Rytov) that are valid only for unrealistically small variations in sound speed and attenuation. Diffraction tomography attempts to reconstruct an image from the scattered acoustic field with consideration of diffraction effects by utilizing approximations to the wave equation. Diffraction tomography received substantial theoretical treatment but with only a few researchers exploring medical applications for its potential to characterize tissue on the basis of physical properties. It is potentially able to account for the inherent diffraction in sound propagation and is not limited by assumptions of straight-line ray geometry. The method involves illuminating an object with ultrasound and measuring a set of scattered wave data around the object.

The approach described in this section used a wave-based diffraction tomography (DT) technique in a clinical prototype system developed in 1994 that addressed many of the shortcomings of previous work. It provided a large field of view (20 cm diameter) with high resolution ($\sim$1 mm) at low acoustic intensities ($<$10 mW cm^2), it was not strongly dependent on operator expertise, it provided a standardized sequential tomographic approach to surveying the entire breast, and it provided quantitative tissue properties in vivo. The methods of image

reconstruction employed were similar to previous diffraction tomography work in which the wave equation for the propagation of sound through a spatially variant medium is solved approximately (Kaveh et al. 1980; Devaney 1982; Wolf 1969). One significant difference is that this method acquired the 360° 2D scatter field around the object in a very short time interval plus it employed much lower frequencies (0.3–1.0 MHz) and continuous wave transmission. The researchers developed several approaches to image reconstruction that are closely tied to the annular array transducer configuration and data acquisition methods (André et al. 1995, 1996).

15.4.1 Clinical DT Prototype Design

This method of diffraction CT used steady-state sound to illuminate the medium from which the amplitude and phase of the scattered sound waves emanating from the medium and object were measured at the perimeter of the field. The system used much lower frequencies than were attempted previously by most researchers. By operating at 1 MHz and below, absorption and phase aberration are diminished permitting simplifications in image reconstruction. Cylindrical geometry of the transducer array allowed a compact design compared to plane-wave systems (Fig. 15.9). The transducer elements emitted a concentric cylindrical beam pattern that, together with the geometry of the receiver array, allowed transformation to a plane wave basis for efficient reconstruction. The toroidal array was designed to ensure adequate sampling of the entire 2D scattered field. The data acquisition system was capable of recording, digitizing at 30 MHz (12 bits) and storing a large amount of acoustic data quickly (<1 s at 0.5 MHz).

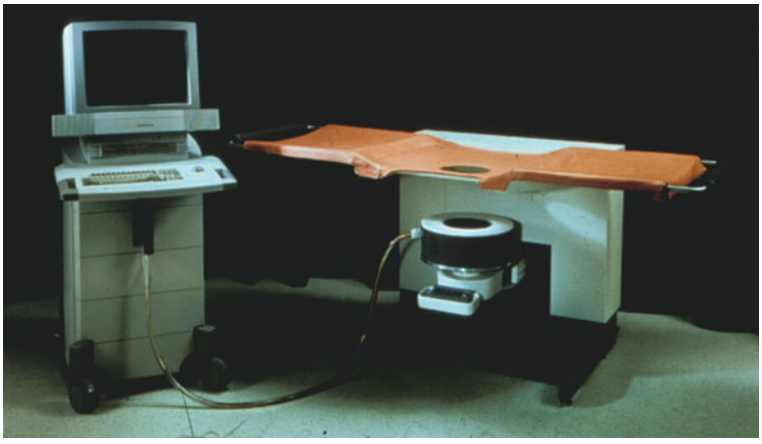

Fig. 15.9 Clinical DT prototype scanning system with annular array mounted on a vertical translation stage below a modified breast biopsy table. From André et al. (1997)

The patient scanning system is shown in Fig. 15.9 in which the cylindrical array is mounted below a modified breast biopsy table. Two separate arrays with 20 cm diameter were developed: 512 elements with center frequency at 0.5 MHz, and 1,024 elements with center frequency at 1.0 MHz. The entire measurement procedure is normally repeated at 10 discrete frequencies, ω_α ($\alpha = 1,2,\ldots,A$) where $A = 10$, spaced at 62.5 kHz intervals from 687 to 1.250 MHz for the 1,024 array. 20 discrete frequencies were typically used with the 512 array, spaced at 31 kHz from 300 to 600 kHz. The arrays had 60 % bandwidth and center frequencies of 1 and 0.4 MHz, respectively, in which the transducers were spaced evenly at slightly less than $\lambda_0/2$ (0.5 mm transducer width with 0.75 mm spacing for the 1 MHz array, 1.0 mm width and 1.5 mm spacing for the 0.5 MHz array). The elements were 12 mm in height to encourage a dipole ($\cos\theta$) pattern of wave propagation and were on a locus of a circle of radius 102 mm in both arrays. The transducers each act in turn as transmitter on a plane (r,θ), while the remaining elements act as receivers (Fig. 15.10). The z-direction is perpendicular to this plane. The full-width half-maximum of the slice sensitivity profile was approximately 8 mm across the field of view. The large 20 cm ring of transducers illuminated the tissue via a heated coupling bath (Fig. 15.9). The acoustic properties and temperature of the bath are adjusted to better match the acoustic properties of tissue and enhance penetration through the skin.

The transmitter is operated in one of two modes: (1) a continuous-wave mode in which single discrete frequencies (ω_α) were transmitted one at a time; (2) a broadband mode in which a periodic signal was used that is timed to repeat in concert with the receiver such that discrete frequency bands may be deconvolved from the measurements. The second procedure provides a rapid way to acquire the equivalent of many (usually 10 or more) discrete frequencies with a single transmission. The desired single- frequency waves are combined in the arbitrary waveform generator with varying phases between the different frequency cycles. This wideband signal was developed experimentally to maximize the peak-to-peak

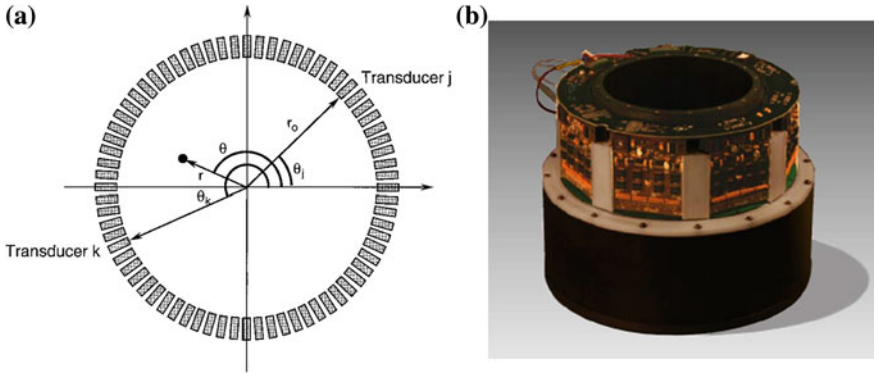

Fig. 15.10 Annular transducer array geometry (**a**) for a cylindrical wavefront emitted by transducer k and received by transducer j. Water tank and array with cover removed (**b**)

transmitted energy at each frequency. The Fourier transform of this wideband signal is a comb-shaped pattern. The acquired information is in the form of an N × N complex matrix, $m_{jk}(\omega_\alpha)$ (j, k = 1,… N), for data acquired at in sonification frequency ω_α. A full set of receiver data for a complete transmit sequence is obtained in approximately 1 s for the 512 array (64 MB) and <3 s for the 1,024 array (128 MB). Detailed description of the data acquisition procedures is given in André et al. (1997).

15.4.2 DT Image Reconstruction

The complex amplitude, $m_{jk}(\omega_\alpha)$ (j, k = 1,… N), of the scattered acoustic wave measured at transducer k due to transmission from transducer j acquired for the medium may be described by the sound speed c(r, θ) and attenuation coefficient μ(r, θ) of the medium. The resulting image is based on the calculation of an approximation of the complex scattering potential, S^α(r, θ), at all locations (r, θ) throughout the slice of the medium (Fig. 15.10a). This algorithm has been described in detail elsewhere (André et al. 1995, 1996) but will be summarized here.

A solution to the wave equation due to single frequency illumination of the medium can be expressed in terms of a two-dimensional integral equation involving the complex scattering potential S^α(r, θ), the position of the transducers (r_0, θ), and the tabulated Hankel (H) and Bessel (J) functions (Devaney 1982), where the radiation pattern of the transducers is approximated well by a linear dipole such that

$$g(|r - r', \theta - \theta'|) = H_0^{(1)'}(k|\rho - \rho'|) \tag{15.1}$$

$g(|r - r', \theta - \theta''|)$ is the free-space Green's function, which describes a source transducer that acts as a dipole transmitter and receiver, ρ is density and k is the wave number. This takes the form

$$m_{jk}(\omega_\alpha) = \sum_{m,n}^{N} H'_m(k_0 r_0) H'_n(k_0 r_0) e^{-im\theta_j - in\theta_k} \int_V J_m(k_0 r) J_n(k_0 r) e^{i\theta(m+n)} S^\alpha(r, \theta) r dr d\theta \tag{15.2}$$

In the above equation, H_n' is the first derivative of the Hankel function of the integer order n representing the antenna pattern of the transmitter j, and H_m' represents the antenna pattern of receiver k. H_n' can be shown by Gegenbauer's addition theorem (Abramowitz and Stegun 1965; Devaney 1982) to be indicative of a dipole antenna pattern for both the transmitters and receivers. This antenna pattern has a complex dipole amplitude with a cylindrically symmetric phase and a magnitude in the imaging plane in the form of cos ϕ where ϕ is the angle from the vector normal to each transducer face. Different transducer radiation patterns may

be accommodated by substituting a weighted sum of monopole, dipole, etc., patterns or by using measured values. $J_m(k_0r)$ and $J_n(k_0r)$ are Bessel functions determined for all values r within the plane (r, θ). Equation 15.2 is derived in the Born approximation, which assumes that the medium is a weak scatterer of acoustic waves and induces small phase-shift variations in the incident wave front. Attenuation and phase shift in tissue are proportional to frequency; attenuation for breast tissue averages about 0.5 dB/cm/MHz while breast tissue exhibits fairly small fluctuations (±8 %) in sound speed. The use of frequencies lower than commonly employed in medical breast ultrasound, 0.5–1.5 MHz compared to 7–15 MHz, helps to constrain the breast properties to a range more appropriate for inversion techniques within range of the Born approximation as illustrated in the simple analysis of Fig. 15.11. The wave number, $k_0 = \omega/c_0$, was set to be the wave vector of the coupling fluid.

Several methods have been described to invert Eq. 15.2 but one of the most efficient methods is backpropagation that can be adapted to the specific geometry of the DT system. This may be viewed as beam forming in which a sound beam is formed in the medium by summing the set of N source transducers (j = 1,2,…,N), such that the signals add coherently at the point (r, θ).

The beam pattern of the transducer elements is removed by transforming the cylindrical data set into a form analogous to plane wave transmitters and receivers:

$$S_{pq}^{\alpha} = \left[\frac{1}{H_m'(k_0r_0)H_n'(k_0r_0)}\right]\sum_{j,k=1}^{N} m_{jk}(\omega_\alpha)e^{-\left(ip\theta_j - iq\theta_k\right)} \tag{15.3}$$

From reciprocity, we expect m_{jk} and S_{pq} to be symmetric matrices. At this point it is possible to filter S_{pq} to reduce the contribution from waves undergoing large diffraction. There is no preferred measurement direction in the transducer array so it can be shown that the convolution in the azimuthal domain is one dimensional such that

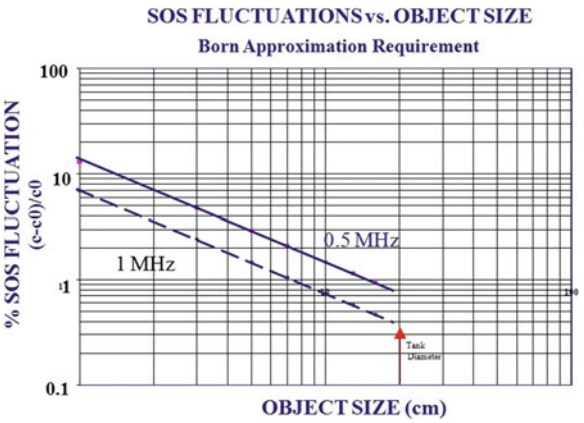

Fig. 15.11 Range of validity for the Born approximation at 0.5 and 1.0 MHz. At these frequencies up to 10 % variation in sound speed is accommodated for objects sizes up to the 20 cm diameter of the arrays (*red arrow*)

$$S_{pq}^{\alpha\prime} = \sum_{n} S_{p+n,q-n} C_n \tag{15.4}$$

where C_n are the filter coefficients in the azimuthal mode domain that simplify to

$$C_n = \frac{4\,k}{\pi} \frac{1}{1-4n^2} \tag{15.5}$$

The backpropagation reconstruction utilizes the filtered azimuthal mode data to obtain the scattering potential or object function $S^{\alpha}(r, \theta)$ in terms of a large azimuthally symmetric set of measured acoustic data $m_{jk}(\omega_\alpha)$, the known positions of the transducers, and tabulated Hankel functions. This process is summarized as follows. First compute the discrete two-dimensional Fourier transform of the filtered data:

$$\tilde{S}^{\alpha}(r,\theta) = \frac{1}{\Im_2\left\{\left[J_0(k_0 r)\right]^2\right\}} \Im_2 \left\{ \sum_{p,q=-N/2}^{N/2} J_p(k_0 r) J_q(k_0 r) e^{-i\theta(p+q)} S_{pq}^{\alpha\prime} \right\} \tag{15.6}$$

The discrete inverse two-dimensional Fourier transform of Eq. 15.6 recovers S^{α},

$$S^{\alpha}(r,\theta) = \Im_2^{-1}\left[\tilde{S}^{\alpha}(r,\theta)\right] \tag{15.7}$$

In Eq. 15.7, $\Im_2$ represents the two-dimensional Fourier transform operation: $g(\kappa, \phi) \equiv \Im_2\{f(r, \theta)\} \equiv f(r, \theta)e^{-i\kappa r\cos(\theta-\phi)}rdrd\theta$, and $\Im_2^{-1}$ represents the inverse Fourier transform: $f(r, \theta) \equiv \Im_2^{-1}\{g(\kappa, \phi)\} \equiv g(\kappa, \phi)e^{-i\kappa r\cos(\theta-\varphi)}\kappa d\kappa d\phi$. This algorithm produces an image or map of $S^{\alpha}(r, \theta)$ with a spatial bandwidth of $2k_0$, which is equivalent to a theoretical quantization limit of $\lambda/4$ or approximately 0.4 mm at 1 MHz in water. The basic steps of the image reconstruction process are shown in the flow chart of Fig. 15.12.

The reconstructed complex scattering potential $S^{\alpha}(r, \theta)$ given by Eq. 15.7 has a real part with an inverse quadratic dependence on the sound speed, $c(r, \theta)$, and an imaginary part with a linear dependence on the attenuation coefficient, $\mu(r, \theta)$. However, for the range of sound speeds found in breast tissue, the real part of $S^{\alpha}(r, \theta)$ can be linearized to reasonable accuracy. The linearized scattering potential, $I^{\alpha}(r, \theta)$, is given by:

$$I^{\alpha}(r,\theta) = -2\omega_{\alpha}^2 \left[\frac{\Delta c(r,\theta)}{c_0^3}\right] - i\omega_{\alpha}\Delta\mu(r,\theta) - \rho(r,\theta)^{1/2}\nabla^2\rho(r,\theta)^{-1/2} \tag{15.8}$$

In Eq. 15.8, $\Delta c(r, \theta) = c(r, \theta) - c_0$ and $\Delta\mu(r, \theta) = \mu(r, \theta) - \mu_0$, which are spatially dependent perturbations from the average sound speed, c_0, and attenuation coefficient, μ_0, of the entire medium including the object and coupling fluid. The attenuation coefficient represents energy loss mechanisms including absorption and scattering of acoustic energy out of the field of view of the transducers.

With this approach it was possible to define different ways of combining multiple reconstructed images $S^{\alpha}(r, \theta)$ acquired at different discrete frequencies ω_α

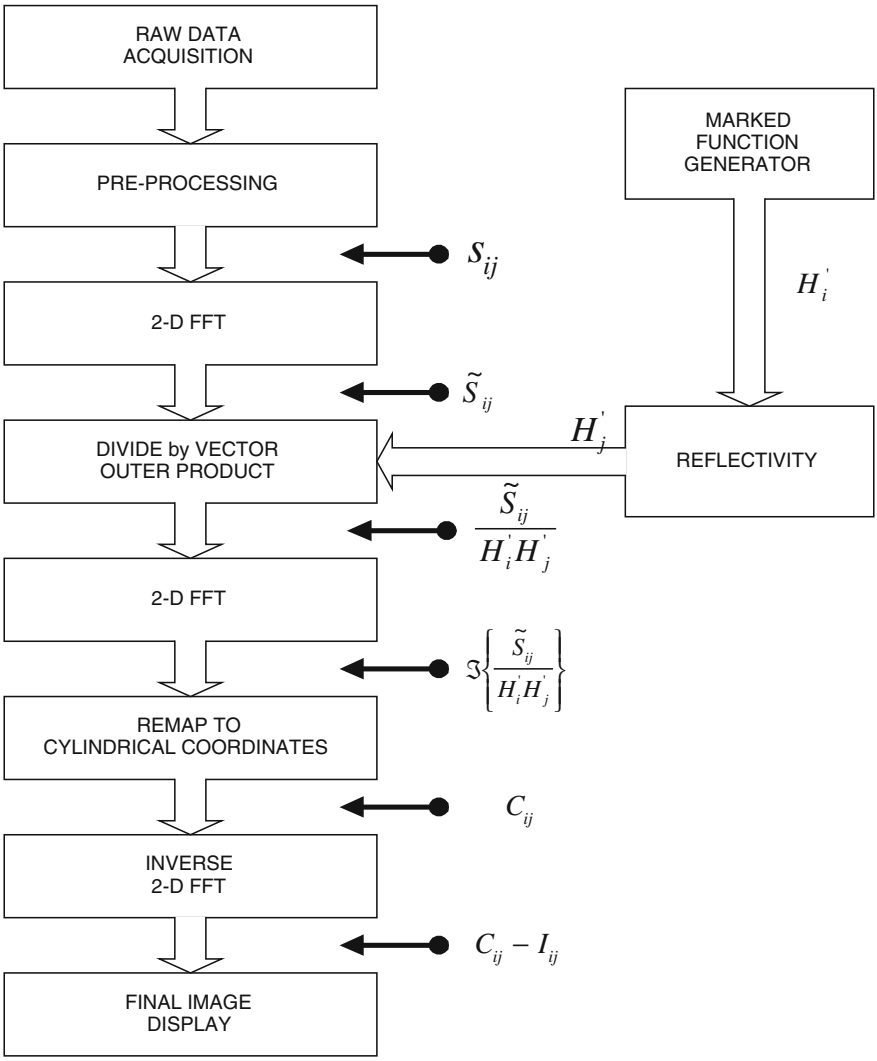

Fig. 15.12 Outline of the basic steps of image reconstruction

($\alpha = 1,2,\ldots,A$). The researchers found that summing the complex images $S^{\alpha}(r, \theta)$ or summing the magnitudes of these complex images reduces image artifacts due to reflections of acoustic energy from the receiver transducer faces and from multiple scattering events within the object being imaged.

As an extension to the above solution that is based in the Born approximation, they developed a hybrid reconstruction scheme that performs phase aberration correction to reduce distortion (André et al. 1997, 1996). This was accomplished by synthesizing pulse data at each point in the image field from a multiple-

frequency acquisition, summed as a Fourier series. These synthetic beams from all transmitters sequentially focus at each point in the object and then propagate back to all receivers. A time-of-flight map, $\tau(r, \theta)$, is calculated to each point in the object for each transmit–receive transducer pair and the attenuation of the pulse peak value relative to the background water bath is determined. These maps are essentially low-spatial frequency images of sound speed and attenuation. A phase correction, $e^{-j\omega\tau(r,\theta)}$, is applied to each single frequency backpropagation image, which results in higher spatial frequency images. The corrected single-frequency images were then summed to reduce aberration artifacts.

15.4.3 DT Results

Forty-five women, both symptomatic and asymptomatic, were successfully imaged with the DT system in a small pilot study. Images for an asymptomatic 65 year old patient with average density breasts were acquired at the same level with both arrays (Fig. 15.13). The real (sound speed), imaginary (attenuation) and scatter density components are displayed left to right. The images are frequency compounded from 330 to 640 kHz for the 0.5 MHz data (top row) and from 630 to 1,200 kHz for the 1 MHz array (bottom row). Fibroglandular tissues appear with bright signal while fat is dark.

A series of sequential tomographic slices for the left breast of a 42 year old subject are shown in Fig. 15.14 acquired with the 1 MHz array. Images were reconstructed from the nipple to maximum posterior level (bottom row to top) with 4 mm overlap at 10 mm intervals. The most posterior slices towards the chest wall in the top row show increasing amounts of retroglandular fat with diminishing bright signals from fibroglandular structures. Figure 15.15 shows polar plots of angular scatter data for the same subject acquired at 0.5 MHz for transmission from a single transducer at 0° acquired in the scan tank medium (a) and the medium plus breast scanned at approximately the middle of the breast (b). The data from this subject reveal high spatial frequency fluctuations that are believed to be acoustical signals possibly due to diffraction effects, multiple scattering and reflections. These data show significant attenuation and energy scattered at angles larger than those subtended by the breast. This suggests that such large-angle scattering is due to compressibility fluctuations, which gives rise to monopole terms. The patient had dense breast tissue on mammography (BI-RADS Category 3) with regions of very dense tissue, scattered microcalcifications but no abnormalities. The shape of scatter amplitude distribution was found to be closely represented by the Rayleigh distribution, suggesting a strong scattering condition. Other patient breasts with higher fat-gland ratios (BI-RADS 1 and 2) were found to exhibit relatively weaker scattering.

The advantages of summing data from multiple frequencies (10) is demonstrated in Fig. 15.16 for a 15 cm uniform saline phantom with sound speed of

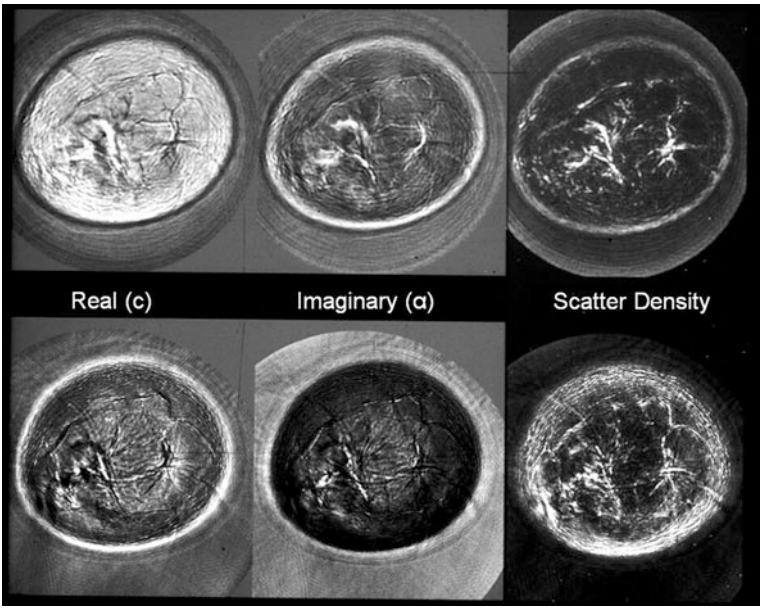

Fig. 15.13 Images for a 65 yo patient with average density breasts acquired with both arrays. *Top row* was acquired with 1 MHz array, *bottom row* with 0.5 MHz array at approximately the same level in the breast

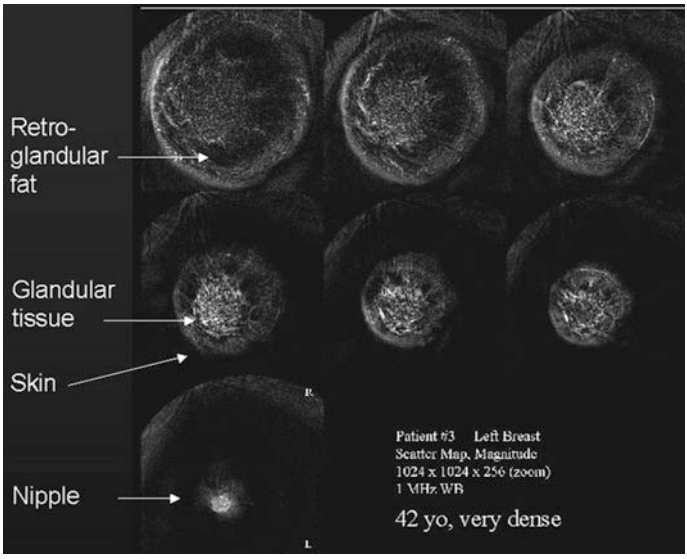

Fig. 15.14 Sequential series of images from a 42 yo subject with dense to very dense breast tissue. 1 MHz array

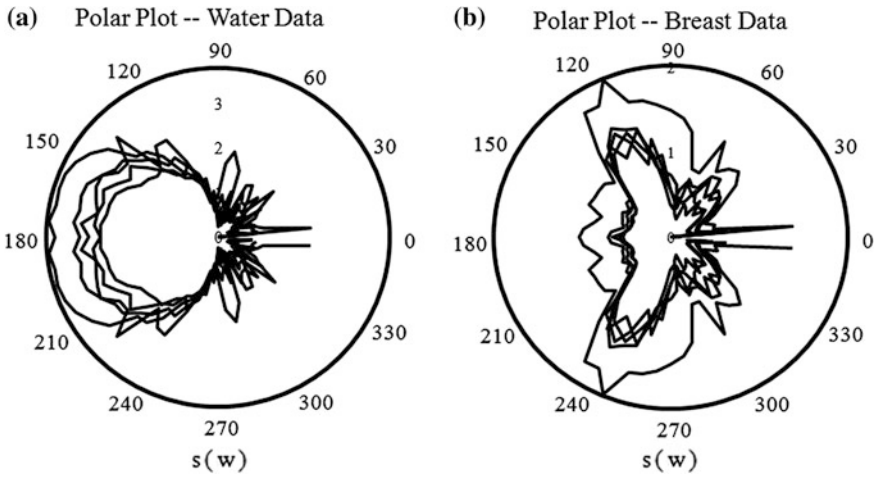

Fig. 15.15 Angular scatter distribution for the same subject with dense breast tissue (scattered fibroglandular density, BI-RADS 3). 0.5 MHz array

1,510 m/s. Non-uniformity is suppressed, the maximum effect of which occurs with frequency separation $\Delta\omega < c_0/D$, where c_0 is the average sound speed in the medium + object, D is the diameter of the field of view, and the total frequency range should be as large as possible. This image was acquired with the 0.5 MHz array.

Tissue contrast (relative units) compared to the water bath medium for sound speed images was measured in eight patients and is plotted in Fig. 15.17. Fat presents low values, fibroglandular tissues that are high in collagen show intermediate to higher sound speed values while the few cancerous masses all had very high values. In phantoms, the minimum sound speed sensitivity was found to be 0.5 %, which provides excellent performance.

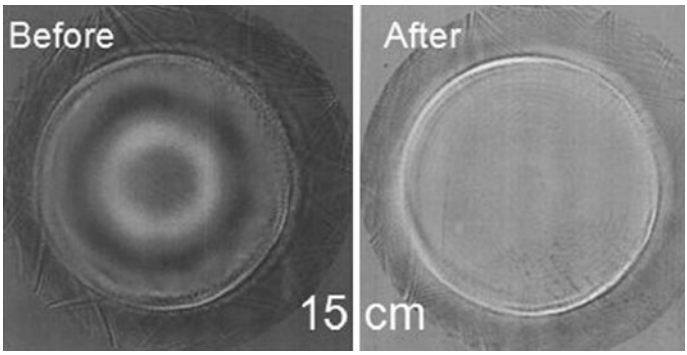

Fig. 15.16 Images from the 0.5 MHz array for a 15 cm diameter saline-filled phantom showing artifact reduction with 10-frequency averaging (*right image*)

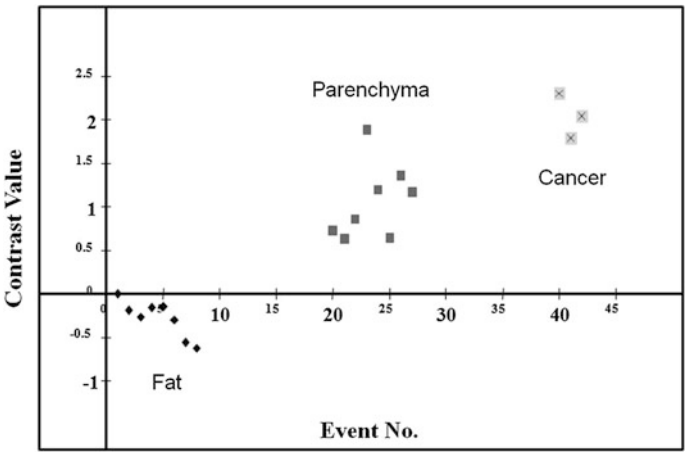

Fig. 15.17 Relative sound speed contrast for fat, fibroglandular (parenchyma) and confirmed cancer masses measured in eight patients

In general, the results of this work demonstrated a DT system sufficiently fast to be practical for clinical research. Image quality was promising despite artifacts inherent with coherent imaging methods and the low transmit power. The system design allowed simplifications in the algorithms for more efficient computation necessary with available computing resources and the researchers developed iterative methods to reduce aberrations and extend the limits imposed by the Born approximation. It was found to provide reproducible sound speed contrast but the methods used to achieve this reduced the accuracy of the attenuation (imaginary) component. It was concluded that the 2D geometric approximations in the algorithms as well as the inability to acquire signals scattered out of plane were significant limitations on performance.

15.5 Inverse Scatter Tomography (IST)

The third stage of development is the introduction of true wave equation based methods, not linear perturbation approximations, as models of ultrasound wave propagation (Berg et al. 2012; Carson and Fenster 2009). The wave equation approach described in this section provides a non-linear model of considerable accuracy, compensates for multiple scattering and provides uniform resolution throughout the image plane. This model is inverted by an iterative simultaneous determination of the breast tissue parameters and internal total fields (Fig. 15.18). Until recently, the mathematical and technical challenges for full-wave 3D IST were so complex that practical results in humans were not realized.

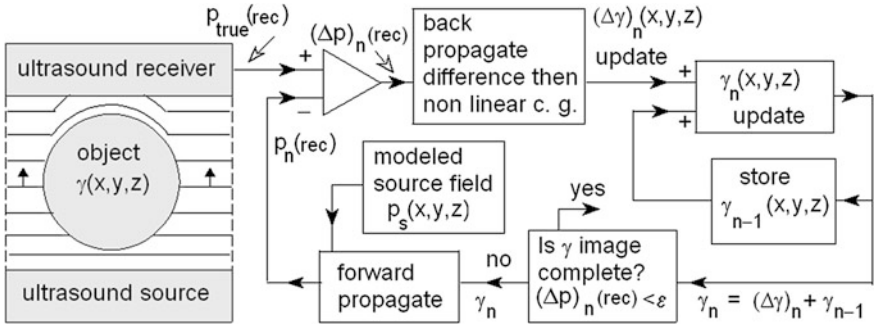

Fig. 15.18 General principle of inverse scatter algorithm

To achieve a solution of the inverse scattering problem the algorithm implements a fast forward solver and concomitant methods for large scale ($\sim$20 million unknowns) minimization of a functional F. The minimization is based on the Ribiere-Polak version of nonlinear conjugate gradients and therefore requires a fast way to calculate the gradient of F and the step length. The inversion algorithm is based on a type of approximate factorization of the Helmholtz wave equation that leads to a form of the phase screen approach (U.S. Patent No. 6,636,584). To solve the numerically ill-conditioned problem of full-wave inversion, increasing discrete frequency data are used and the number of iterations can be reduced by preconditioning to a practical level of 5–8 to achieve a 5 % residual. The method does not account for density variations but for scatter in the forward direction this approximation has proven reasonable. Detailed description of the 2D and 3D IST algorithm is published elsewhere (Borup et al. 1992; Wiskin et al. 2007, 2011, 2012; Johnson et al. 2007).

15.5.1 IST Theory

The attainment of an inversion or imaging algorithm that utilizes the full waveform and the inherent nonlinearity of the inversion process in a potentially useful time frame has been lacking. Furthermore, for medical application the inversion should take place on a computational engine that can accompany the data acquisition device, and be reasonably inexpensive, if the device is to be clinically useful as a self-contained device.

The inverse scattering algorithm is based on the minimization of the functional F, a function of the object function $\gamma(\mathbf{x}) \equiv (1/k_o)(k(\mathbf{x}) + i\alpha(\mathbf{x}))$ where $k_o \equiv \omega/c_o$ and $k(\mathbf{x}) \equiv \omega/c(\mathbf{x})$ are the wave-numbers in water and inhomogeneous tissue, respectively, at frequency $\omega = 2\pi f$ and α is the attenuation coefficient in Np/mm.

$$\min F_{\omega_j}(\gamma(\mathbf{x})) = \min \frac{1}{2} \sum_{\substack{\theta=1,\ldots N_{views} \\ l=1,\ldots,N_{levels}}} \overline{\mathbf{r}^l_{\omega_j\theta}(\gamma)} \mathbf{r}^l_{\omega_j\theta}(\gamma) \tag{15.9}$$

at successive frequencies, ω_j, $j = 1, \ldots N_{freq}$. We proceed from low frequencies to high frequencies to avoid local minima. We image at 0.35, 0.4, 0.45, 0.5, 0.6, 0.7, and 0.8 MHz successively for the 2D case, and 0.5, 0.6, 0.7, 0.8, 0.9, 1.0, 1.1, 1.2, and 1.25 MHz successively for the 3D volume image. The vectors

$$\mathbf{r}^l_{\omega\theta}(\gamma) \equiv \left(\hat{\mathbf{d}}^l_{\omega\theta}(\gamma) - \mathbf{d}^l_{\omega\theta} \right) \in C^{N_R} \tag{15.10}$$

represent the residual between the predicted field, $\hat{\mathbf{d}}^l_{\omega\theta}(\gamma)$, and the measured field, $\mathbf{d}^l_{\omega\theta}$, at each receiver position, for each transmitter position, θ, level l, and at the fixed frequency ω. Note that this functional involves all views and all levels simultaneously; that is, it is a true 3D algorithm.

The algorithm at the highest level is described in (Wiskin et al. 2007). It is a series of updates to γ. $\gamma^{(n+1)} = \gamma^{(n)} + \alpha_n \mathbf{d}_n$, where the descent direction $\mathbf{d}_n \equiv -\mathbf{g}_n + \beta_n \mathbf{d}_{n-1}$, and where $\mathbf{g}_n$ is the gradient, β_n is the Ribiere-Polak coefficient ($\beta_0 = 0$),

$$\beta_n \equiv \frac{(\mathbf{g}_n - \mathbf{g}_{n-1})^T \mathbf{g}_n}{\|\mathbf{g}_{n-1}\|^2} \tag{15.11}$$

and α_n is the step-length. The calculation of the step-length and the gradient are detailed below.

15.5.1.1 Initial Estimates

Due to the minimization nature of the algorithm an initial estimate is required. First a time of flight algorithm is used to create a series of initial distributions for speed of sound and attenuation *at each level.* These initial estimates are used in a series of 2D inverse scattering algorithms to create a series of 2D inverse scattering images at each level, which are the distributions that minimize the functional for *one particular level, l.* These 2D images are then concatenated together to form a 3D volume. The 3D volume is the *starting estimate* for the full 3D inverse scattering algorithm. The 3D algorithm is required to account for energy that is refracted or scattered out of plane; when ignoring these signals, the 2D-algorithm gives an anomalously high result for the attenuation estimate.

15.5.1.2 Forward Problem

As mentioned above, a very fast solution of the forward problem is required. To achieve this we rewrite the Helmholtz equation (15.44):

$$\frac{\partial^2 p(\mathbf{x})}{\partial x^2}+\frac{\partial^2 p(\mathbf{x})}{\partial y^2}+\frac{\partial^2 p(\mathbf{x})}{\partial z^2}+(k(\mathbf{x})+i\alpha(\mathbf{x}))^2 p(\mathbf{x})=0 \tag{15.12}$$

$$\text{as} \qquad [(A+iB)(A-iB)-i[B,A]]p(\mathbf{x})=0 \tag{15.13}$$

where: $A \equiv \frac{\partial}{\partial x}$, is a partial differential operator, and $B \equiv \sqrt{\frac{\partial^2}{\partial y^2}+\frac{\partial^2}{\partial z^2}+k^2(x,y,z)}$ is a pseudo-differential operator. $[B,A]$ is the commutator of these operators.

Under the assumption that this commutator can be ignored, we can approximately 'factor' the Helmholtz equation to yield (15.4):

$$\frac{\partial}{\partial x}p(x,\mathbf{r}_\perp)=i\mathbf{H}(x,\mathbf{r}_\perp)p(x,\mathbf{r}_\perp) \tag{15.14}$$

a 'Schroedinger' equation in 'time' x, with the unusual "Hamiltonian",

$$\mathbf{H}(x,\,\mathbf{r}_\perp)=\sqrt{\frac{\partial^2}{\partial y^2}+\frac{\partial^2}{\partial z^2}+k^2(x,\,y,\,z)} \tag{15.15}$$

in transverse co-ordinates $\mathbf{r}_\perp \equiv (y,z), x$ (the direction of propagation) plays the role of time.

A symbolic solution for the propagator from initial state (wave field) at x_o to final state (wave field) at x, is given as the phase-space path integral:

$$\left\langle p(x,\mathbf{r}_\perp)\middle|p\left(x^o,\mathbf{r}_\perp^o\right)\right\rangle=\int D\mathbf{r}_\perp(x)\int D\mathbf{p}_\perp(x)e^{iS(\mathbf{r}_\perp,\mathbf{p}_\perp)} \tag{15.16}$$

with "action", $S(\mathbf{r}_\perp,\mathbf{p}_\perp)\equiv\int_{x^o}^{x}dx\left(\mathbf{p}_\perp\frac{d\mathbf{r}_\perp}{dx}-\mathbf{H}(x,\mathbf{r}_\perp,\mathbf{p}_\perp)\right)$.

Discretizing the 'time' from x_o to x, $x_0<x_1<\cdots<x_{N-1}<x_N<x_{N+1}=x$, and utilizing standard properties of the exponential gives for the propagator:

$$\prod_{j=1}^{N}\int d\mathbf{p}_j e^{i\mathbf{r}_{j+1}\mathbf{p}_j}e^{-i\mathbf{H}\left(x,\mathbf{r}_j,\mathbf{p}_j\right)\Delta x}\int d\mathbf{r}_j e^{-i\mathbf{r}_j\mathbf{p}_j} \tag{15.17}$$

We approximate this with the following form of the propagator acting on the initial field at x_o: $p\left(x_o,\mathbf{r}_o^\perp\right)$, to give the total field at the receivers:

$$p\left(x_N,\mathbf{r}_N^\perp\right)=\prod_{j=1}^{N}t\left(x_j,\mathbf{r}_\perp\right)\odot\mathbf{F}^{-1}P\odot\mathbf{F}p\left(x_o,\mathbf{r}_o^\perp\right) \tag{15.18}$$

The $\odot$ indicates element-wise multiplication of two matrices: i.e. if $A_{\lambda\mu}$, $P_{\lambda\mu}$ are components of 2D matrices, $(P\odot A)_{\lambda\mu}\equiv\left(P_{\lambda\mu}A_{\lambda\mu}\right)$. F indicates Fourier Transform. P is the 2D matrix with elements, $P_{\lambda\mu}\equiv e^{i\varepsilon\sqrt{k_0^2-(\lambda\Delta_k)^2-(\mu\Delta_k)^2}}$, ε is step length in x, Δ_k is step length in transform space: k_y, k_z, and

$$t\left(x_j,\mathbf{r}_\perp\right)\equiv t_j(y,z)\equiv e^{i\varepsilon\left(k\left(x_j,y,z\right)-k_0\right)}\equiv e^{i\varepsilon k_0\left(\gamma\left(x_j,y,z\right)-1\right)} \tag{15.19}$$

is the "phase mask" element-wise multiplication operator discussed in U.S. Patent No. 6,636,584.

15.5.1.3 Gradient of the Functional *F*

The Polak-Ribiere version of the nonlinear conjugate gradient algorithm requires the gradient of functional *F:*

$$\frac{\partial}{\partial \overline{\gamma}} F(\gamma) = \sum\nolimits_{l\theta} \left(\overline{\frac{\partial}{\partial \gamma} \mathbf{r}_{l\theta}} \right)^T \mathbf{r}_{l\theta} \equiv \overline{J}_{\omega}^T \mathbf{r} \tag{15.20}$$

where $J \equiv \frac{\partial \mathbf{r}_{l\theta}}{\partial \gamma}$ is the Jacobian operator. This is obtained in the following manner. $\delta \gamma_j^{\omega\theta} = \mathbf{v}_j \odot f_{\mathbf{r}_{\omega\theta}}^j$ is the contribution to the gradient, from view angle θ and *x-coordinate, x_j*. It is the point-wise product of two 2-dimensional arrays of size (N_y, N_z). viz., $\mathbf{v}_j \equiv \mathbf{F}^{-1} P \odot \mathbf{F} p\left(x_{j-1}, \mathbf{r}_{j-1}^{\perp}\right)$, the total field at propagation distance *j−1,* propagated through water, to propagation distance *j*. $f_{\mathbf{r}_{\omega\theta}}^j$ is the field at x_j, resulting from treating all receivers, at tomographic view angle θ, as transmitters, at frequency ω. The strength of each 'transmitter' is: $f_{\mathbf{r}_{\omega\theta}}^N \equiv \overline{\delta \mathbf{f}}_N$, i.e., the difference between the measured and predicted fields at the receivers, and we recursively define $f_{\mathbf{r}_{\omega\theta}}^j = \mathbf{F}^{-1} \overline{P} \odot \mathbf{F} \overline{\mathbf{t}}_j f_{\mathbf{r}_{\omega\theta}}^{j+1}$, for $j = N - 1,\ldots,0$.

15.5.1.4 Step Length Calculation for Ribiere-Polak Conjugate Gradients

Step length $\alpha_n \approx \frac{\mathbf{g}_n^T \mathbf{d}_n}{\|J_n \mathbf{d}_n\|^2}$, $\mathbf{d}_n$ is the RP descent direction. $\mathbf{g}_n$ is the gradient of the functional *F,* and $J \equiv \frac{\partial \mathbf{r}_{l\theta}}{\partial \gamma}$is the associated Jacobian.

The action of the Jacobian on the descent direction is given by

$$J_n \mathbf{d}_n = \left[\frac{\partial \mathbf{r}_{l\theta}}{\partial \gamma} \right] \mathbf{d} = \delta \mathbf{p}_N \tag{15.21}$$

where: $\delta \mathbf{p}_j = \mathbf{A} \mathbf{p}_{j-1} \odot \delta \mathbf{t}_j + t\left(x_j, \mathbf{r}_{\perp}\right) \odot \mathbf{A}\left(\delta \mathbf{p}_{j-1}\right)$, $j = 1,..,N$, and where $\mathbf{A} \equiv \mathbf{F}^{-1} P \odot \mathbf{F}$ propagates a field a distance ε through water, and $\delta \mathbf{t}_j\left(\mathbf{r}^{\perp}\right) \equiv i\varepsilon k_0 \mathbf{t}_j(y,z) \delta \gamma\left(x_j, y, z\right)$ from the definition of the phase mask $\boldsymbol{t}_{\mathrm{j}}$.

Having determined the step length and descent direction the update is given by

$$\gamma^{(n+1)} = \gamma^{(n)} + \alpha_n \mathbf{d}_n \tag{15.22}$$

15.5.2 IST/RT Scanner

A practical scanner employing IST imaging was developed by Techniscan Medical Systems (now by CVUS LLC, Salt Lake City, UT) (Greenleaf et al. 1974, 1975, 1978; Glover and Sharp 1977). The current scanner that is the subject of this section was employed in clinical research at the University of California, San Diego (UCSD), Mayo Clinic, Rochester, MN, and University of Freiburg, Germany to evaluate clinical feasibility of using IST and RT to analyze and detect breast masses as well as monitor changes due to therapies. All of the data presented here are from UCSD where the majority of the work was done.

The TMS scanner (Fig. 15.19) provides an automated, standardized scan of the whole breast nearly independent of operator expertise. The patient lies prone with her breast pendant but docked to a retention rod in a controlled 31 °C water bath within the field of view of several transducer arrays. The IST transmitter and receiver array rotate around 360° to collect 180 tomographic views of ultrasound wave data (Fig. 15.20). The transmitter emits broad-band planar pulses (0.3–2 MHz) while the receiver array, comprised of 1,536 elements in 8 vertical rows, digitizes the time signal. Total scan time is ∼10–20 s per level, ∼8 min for the average breast. 3D transmission and aberration-corrected RT reconstructions are accomplished in ∼40 min employing 2 nVidia GPUs for a portion of the process.

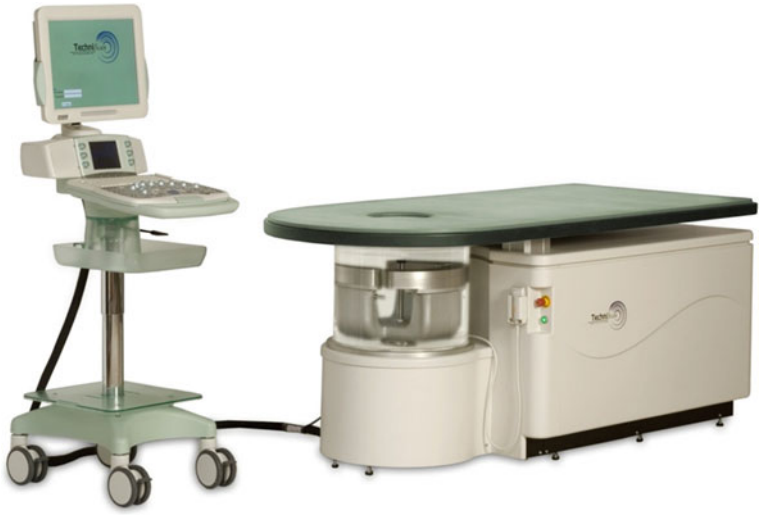

Fig. 15.19 IST/RT scanner with transducer arrays in water tank

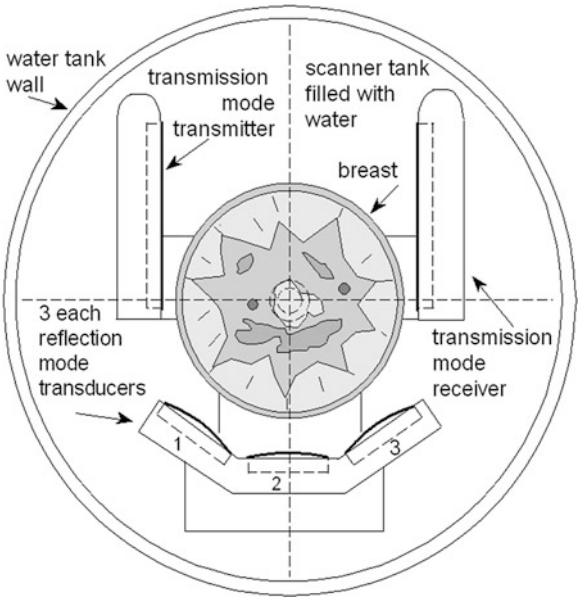

Fig. 15.20 IST/RT transducers arrangement. 1, 2, 3 are the reflection transceivers coincident with the transmission arrays

15.5.3 Reflection Tomography (RT)

The scanner includes a set of three transceiver arrays that are coincident with the transmission arrays to simultaneously acquire conventional B-scan data. The arrays have bandwidths of ~2–8 MHz and are focused at depths of 2.5, 4.0 and 7.5 mm to provide complete depth of coverage of the breast. The three coincident RT arrays (3.6 MHz center frequency, 80 % bandwidth) spaced at 48° are angled upward at 12° to access the chest wall. A high-resolution RT algorithm was developed that utilizes the sound speed image to correct for refraction and attenuation images to adjust amplitude along the ray. The resulting backprojected RT image is a 360° B-scan image compounded from 60 views. The speed of sound and attenuation images resulting from the 3D inverse scattering algorithm are used to correct for refraction effects in the reflection algorithm. The canonical ray-tracing equations derived from the eikonal equation

$$\frac{d}{ds}\left(n\frac{d\mathbf{r}}{ds}\right) = \nabla n,\ n(\mathbf{x}) = c_o/c(\mathbf{x}) \tag{15.23}$$

are solved to give the energy path corrected for refraction due to speed variation. The attenuation images are used to adjust the displayed amplitude of the back-scattered energy along the computed ray.

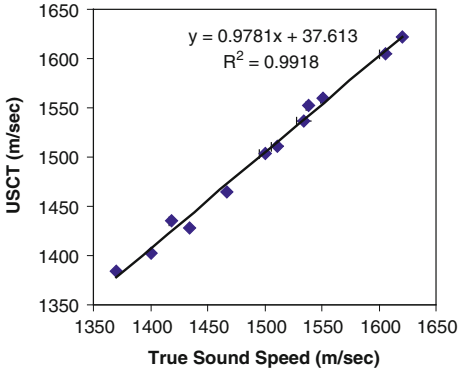

Fig. 15.21 Measured sound speed accuracy. Minimum detectability is ~7.5 m/s

15.5.4 IST and RT Results

15.5.4.1 Scanner Performance

2D reconstruction is completed in seconds, while the full 3D reconstruction is accomplished in ~24 min for average size breast using 2 GPUs. Image quality is excellent with resolution measured as FWHM of LSF of 0.8 mm for RT and 1.5 mm for IST. As shown in Fig. 15.21 sound speed detectability is 7.5 m/s and is highly linear from 1,325 to 1,700 m/s ($R^2 = 0.992$). Sound speed is a function of tissue stiffness, analogous to but not equal to bulk modulus. Attenuation tomograms are a function of tissue structure and composition while providing image contrast over a wide range (0–4 dB/cm/MHz) to assist in classification of masses.

Reflection tomography provides approximately twice the in-plane resolution as the transmission IST images as expected from theory. Image artifacts from compounding 60 views during 360° rotation are greatly reduced by the refraction

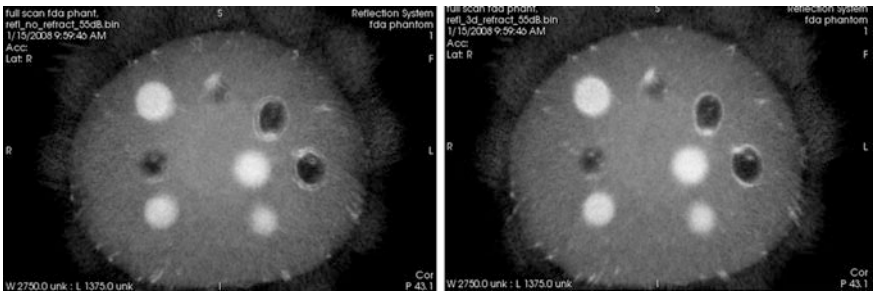

Fig. 15.22 Breast shaped urethane phantom scanned and reconstructed with RT algorithm. The *right image* is with refraction correction using the IST sound speed map while the *left image* is without

correction as shown in Fig. 15.22 for a urethane phantom with a range of inclusions (breast size and shape but not entirely tissue equivalent).

15.5.4.2 Patient Study Population

Female patients recruited to the IRB-approved protocol were referred for a diagnostic breast sonogram as the result of prior findings on mammography, physical exam or previously known conditions. The purpose of the study was to measure a range of tissue properties in women with widely varying breast sizes and mammographic densities, to assess reproducibility of findings and to examine depiction and quantitative properties of masses confirmed by biopsy for suspicious lesions or long-term follow-up for benign findings in comparison to hand-held sonography. The statistical design was to assess equivalence to sonography (93 % power).

15.5.4.3 Clinical Evaluation

Although more than 450 patients have been scanned with versions of IST in the past 5 years, under the current IST/RT protocol 172 patients with an age range of 19–78 years were scanned by the end of 2011, including thorough validation with other clinical findings and long-term follow-up (André et al. 2008; Wiskin et al. 2011; Callahan et al. 2007). The distribution of lesions imaged is as follows: 21 % simple cysts, 17 % complicated cysts, 36 % various solid benign, 26 % cancers, 12 no findings. By study design, this mix of cases very closely matched the three-year average of cases in the UCSD diagnostic breast imaging clinic. Mass sizes ranged from 2–39 mm and there was good agreement in size ($R^2 = 0.7$) between sonography and IST. Not surprisingly, the 3D representation of IST allowed a more accurate representation of the maximum mass diameter where sonography normally only reports radial and anti-radial dimensions. Even more importantly, for 13 patients who also had contrast enhanced MRI there was nearly perfect agreement of size, shape and margins to the IST sound speed images. This high correlation to MRI, which presently serves as the standard for delineating the margins and extent of cancerous breast masses, is a promising opportunity for IST to impact patient care with a much less expensive, less invasive but equivalent imaging modality.

The general quantitative IST attributes of masses can be summarized as follows:

- Simple cysts: low sound speed compared to water, low attenuation
- Complicated cysts: low to intermediate sound speed compared to water, low attenuation
- Solid benign masses: higher sound speed and attenuation
- Malignancies: highest sound speed and attenuation

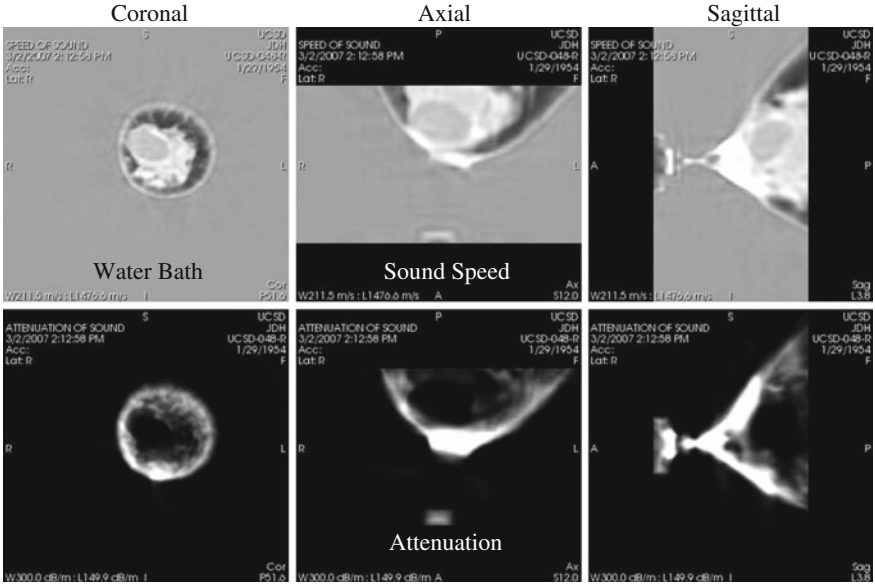

Fig. 15.23 Simple cyst in the right breast

The highest sound speed values that were measured in any patient were all associated with malignant masses, never with normal structures or benign masses. In addition, the three sets of IST/RT images provide reproducible information about mass shape, margins, volume, architectural distortion, texture, relative echogenicity, etc.

A sample of the range of findings found in patients is presented in the following sections. Images are usually presented to the Radiologist in rows with sound speed at the top in vertical columns of coronal, axial and sagittal views from left to right as shown in Fig. 15.23.

15.5.4.4 Research Subject: Simple Cyst

The patient is a 57 year-old female with history significant for profound nipple discharge of the left breast. The images in Fig. 15.23 above are of the right breast, which had a negative biopsy five years prior to the IST scan. The patient complained of a palpable abnormality on the right lasting for approximately one month. A mass was detected in the retroareolar region on mammography and was confirmed by sonogram to be cystic. USCT shows a large mass with distinct margins readily seen just posterior to the nipple. The sound speed values of the mass (upper row Fig. 15.23) are slightly higher (1,540 m/s) than that of water (1,510) while the attenuation images show a black void representing low attenuation values consistent with that of fluid ($\sim$0 dB/cm) (Fig. 15.23).

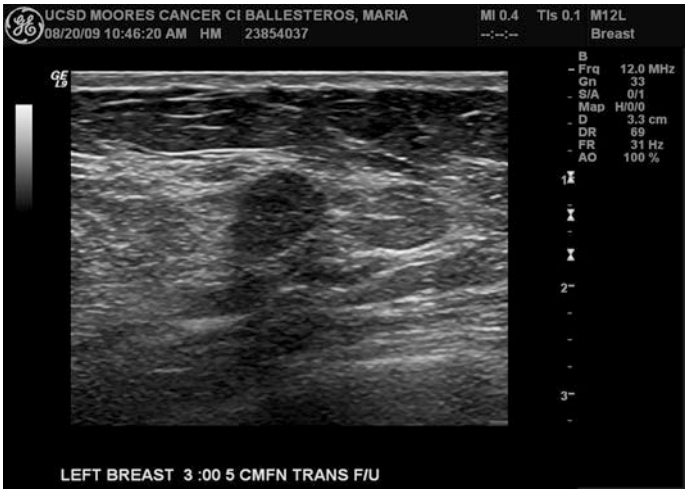

Fig. 15.24 Biopsy confirmed fibroadenoma, palpable mass at 3:00, 5 cm from nipple, 10 mm solid

15.5.4.5 Research Subject: Benign Fibroadenoma

In this case a 40 year old subject had a persistent biopsy-confirmed fibroadenoma in the left breast that was followed with a series of diagnostic sonograms. The mass was 10 mm, it was hypoechoic on sonography with posterior shadowing, distinct margins consistent with a solid mass, and it was found 5 cm from the nipple at the 3:00 position (Fig. 15.24). On IST/RT (Fig. 15.25) the mass is seen at 3:00, 8 × 9 × 6 mm diameter with intermediate sound speed (1,560 m/s), intermediate attenuation (1.6 dB/cm/MHz), and hypoechoic with distinct margins on RT.

15.5.4.6 Research Subject: Invasive Ductal Carcinoma

This case was of a 33 year old woman, with no family history of cancer, seen for a lump or thickening of the breast. Mammography (Fig. 15.26, left) showed a heterogeneously dense, spiculated 2 cm mass with malignant-appearing micro calcifications in the left breast in the middle outer quadrant. The sonogram (Fig. 15.26, right) shows at the 1:00 position in the breast, 2 cm from the nipple an irregular, heterogeneous, highly suspicious mass with angular margins and abrupt interface, 1.9 × 1.2 cm in diameter. Biopsy confirmed it was invasive ductal carcinoma.

The IST sound speed and RT images (Fig. 15.27) show the mass at 1:00 in the coronal view, 2.2 × 1.1 × 1.6 cm, corresponding well to the measurements by sonogram. The mass has very high sound speed (mean 1,570 m/s), bright compared to water, high attenuation (2.3 dB/cm/MHz) and appears hypoechoic with spiculated margins and irregular shape on RT with architectural distortion similar

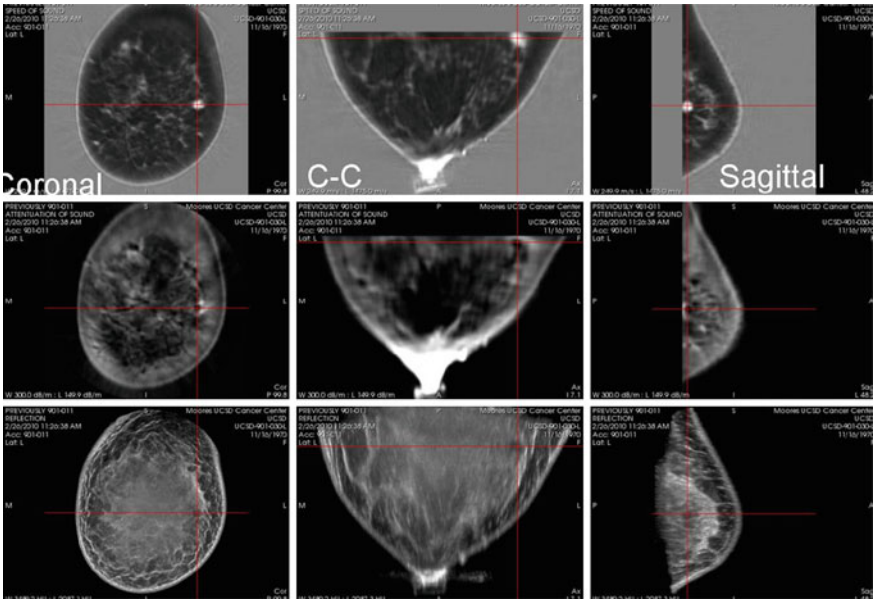

Fig. 15.25 UST images with sound speed on the *top row*, attenuation on the middle row, reflection tomography on the *bottom row*. The fibroadenoma is seen as a mass, marked by the *red cross* hairs, with high sound speed at 3:00 on the coronal view, intermediate attenuation and hypoechoic on the reflection tomogram

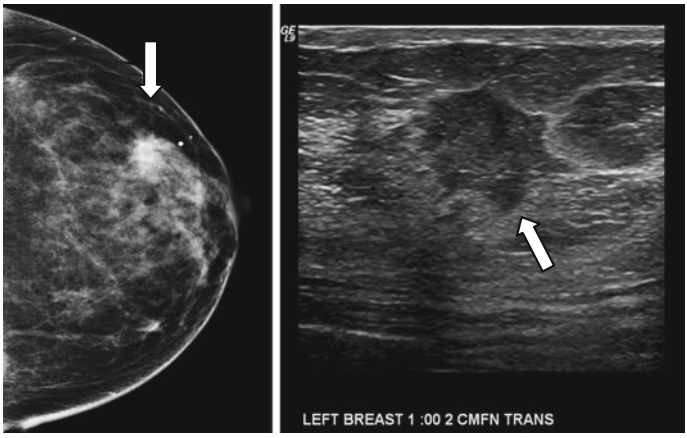

Fig. 15.26 Mammogram (*left*), sonogram (*right*)

to the mammogram. Precisely as the IST/RT images, the coronal T1-weighted contrast-enhanced MRI (Fig. 15.28, right) showed a mass in the same location with dimensions 2.1 × 1.7 × 1.8 cm. The fluid-filled void from the core biopsy is visible in both sound speed and MR images.

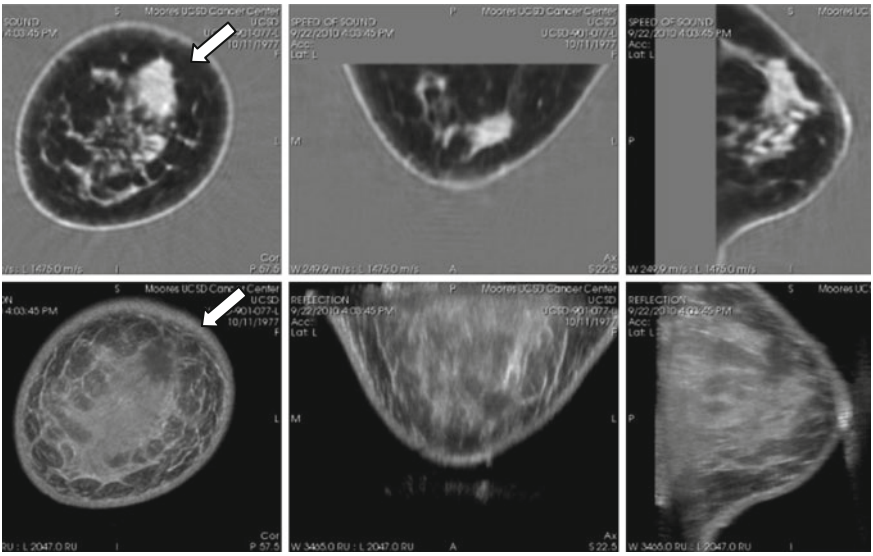

Fig. 15.27 Sound speed IST in *upper row*, RT *lower row*. Coronal (*left*), cranio-caudal (*middle*), sagittal (*right*)

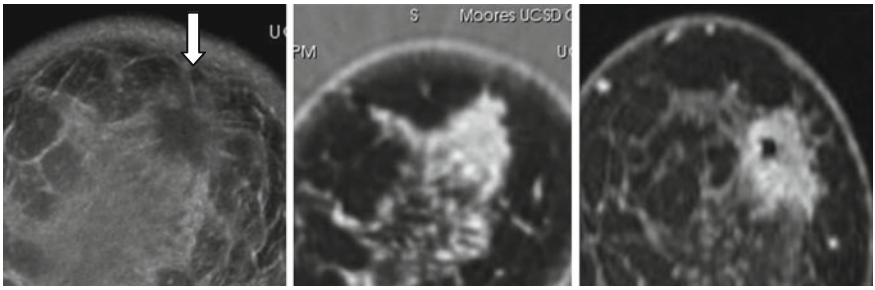

Fig. 15.28 RT (*left*), sound speed (*middle*), T1 weighted MRI (*right*)

As shown in Fig. 15.29, normal tissues and masses may be characterized by their acoustic properties. Fatty normal tissues (indicated by unfilled diamonds) are consistently very low sound speed with lower attenuation, therefore, fatty tissues appear dark on sound speed and attenuation images. Fibroglandular tissues (shown by the clear triangles) have intermediate sound speed and attenuations values. Simple cystic masses (shown by green circles) have consistently low attenuation with intermediate sound speed close to that of water, while complex cystic masses (shown by the blue circles) are higher in attenuation. Solid benign masses such as fibroadenomas (shown by the purple triangles) are wide ranging in sound speed.

To date, cancers (shown by the red squares) have shown both high sound speed (highest sound speed values ever measured were confirmed cancers) and high

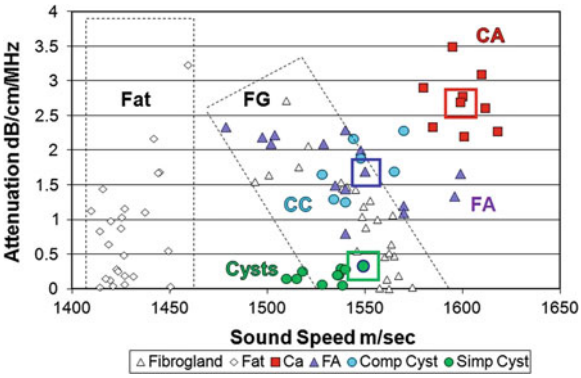

Fig. 15.29 Summary of results for sound speed vs. attenuation values for normal tissues in 75 subjects. Data for the three sample cases above are indicated by the *red*, *blue* and *green boxes*

attenuation. Clearly there is some overlap in the acoustic properties of masses, but these data show promise that the quantitative WBU images may be helpful in differentiating masses.

A 98 % agreement that a mass was present in the correct location was found between IST/RT and sonography. It was determined from comparison to mammography and physical exam that three masses were outside the field of view of IST, either immediately at the chest wall or in the upper outer quadrant in the axillary tail. No statistically significant differences were observed between the two modalities in terms of sensitivity and specificity.

15.5.5 Summary

The attributes of whole breast IST and RT present the following potential clinical advantages: (1) operator independence with automated scanning, (2) true anatomic breast positioning, i.e., no breast compression or distortion, (3) no ionizing radiation, (4) true quantitative 3D imaging algorithms (not just stacked 2-D images), (5) accurately registered 3D IST and RT images, (7) global views of both breasts for detailed contralateral and serial comparisons, and (8) ability to provide quantitative tissue characteristics that have thus far, not been available in medicine. These characteristics provide unique advantages in the clinical setting for applications including, but not limited to, repeat breast imaging that is safe and cost-effective, whole-breast screening for high-risk women, young women or women with dense breasts, accurate volumetric analysis for detailed surgical planning, and monitoring over time of response to surgery and therapy.

15.6 Conclusion

USCT has long history so it is a fair question to ask if the technology will soon be ready for clinical use. The image quality, speed and performance of the IST/RT scanner described in Sect. 2.5 appear to be suitable and practical enough to play a role in breast cancer detection, diagnosis and management. Certainly in the very near future it will be ready for thorough objective clinical testing and with clinical success may come commercial viability. In addition, a new scanner is imminent from Delphinus Medical Technologies (Detroit, MI) that encompasses many design changes over the early prototype described in (Duric et al. 2005, 2006, 2007), which should lead to significant improvements in image quality. It is an interesting and important time for USCT, with perhaps an opportunity to finally advance from the laboratory to routine clinical use.

Acknowledgments We gratefully acknowledge the support and contributions of Melissa Ledgerwood, B.S., Melanie Aiken, B.A., Laura Brogoch, B.S., Karleen Callahan, Ph.D. and the National Institutes of Health, National Cancer Institute SBIR Program and Academic-Industry Partnership Program.

References

Abramowitz A, Stegun I (1965) Handbook of mathematical functions. Dover Publications, New York, p 363

ACR (2011) Practice guideline for the performance of a breast ultrasound examination. American College of Radiology, Reston

American Cancer Society (2011). Breast cancer facts & figures 2011–2012. American Cancer Society, Inc, Atlanta

Andre MP, Galperin M, Berry A, Taylor A, Ojeda-Fournier H, O'Boyle M, Olson L, Comstock C (2011) Performance of a method to standardize breast ultrasound interpretation using image processing and case-based reasoning. Acoust Imaging 30:3–10

André MP, Martin PJ, Otto GP, Olson LK, Barrett TK, Spivey BA, Palmer DA (1995) A new consideration of diffraction computed tomography for breast imaging: Studies in phantoms and patients. Acoust Imaging 21:379–390

André MP, Janée HS, Otto GP, Martin PJ, Jones P (1996) Reduction of phase aberration in a diffraction tomography system for breast imaging. Acoust Imaging 22:151–157

André M, Janee H, Otto G, Martin P (1997) High speed data acquisition in a diffraction tomography system with large-scale toroidal arrays. Int J Imaging Syst Technol 8(1):137–147

André M, Barker C, Sekhon N, Wiskin J, Borup D, Callahan K (2008) Pre-clinical experience with full-wave inverse scattering for breast imaging: sound speed sensitivity. Acoust Imaging 29:73–80

Baker J, Kornguth P, Soo M et al (1999) Sonography of solid breast lesions: observer variability of lesion description and assessment. AJR 172:1621–1625

Berg W, Blume J, Cormack J et al (2006) Operator dependence of physician performed whole breast US: lesion detection and characterization. Radiology 241:355–365

Berg WA, Blume JD, Cormack JB et al (2008) Combined screening with ultrasound and mammography vs mammography alone in women at elevated risk of breast cancer. JAMA 299:2151–2163

Berg W, Cosgrove DO, Doré CJ et al (2012a) Shear-wave elastography improves the specificity of breast US: The BE1 multinational study of 939 masses. Radiology 262(2):435–449

Berg W, Zhang Z et al (2012b) Detection of Breast Cancer with addition of annual screening ultrasound or a single screening mri to mammography in women with elevated breast cancer risk. JAMA 307(13):1394–1404

Borup DT, Johnson SA, Kim WW, Berggren MJ (1992) Nonperturbative diffraction tomography via Gauss-Newton iteration applied to the scattering integral equation. Ultrason Imaging 14(1):69–85

Brogoch L, André M, Ledgerwood M, Ojeda-Fournier H et al (2010) Reader variability and predictive value of breast imaging reporting and data system descriptors for lesions in breast sonography. J Ultrasound Med 29:S47

Callahan KS, Borup DT, Johnson SA, Wiskin J, Parisky Y (2007) Transmission breast ultrasound imaging: representative case studies of speed of sound and attenuation of sound computed tomographic images. Am J Clin Oncol 30(4):458–459

Carson PL, Fenster A (2009) Anniversary paper: evolution of ultrasound physics and the role of medical physicists and the AAPM and its journal in that evolution. Med Phys 36(2):411–428

Carson P, Meyer C, Scherzinger A, Oughton T (1981) Breast imaging in coronal planes with simultaneous pulse-echo and transmission ultrasound. Science 214:1141–1143

Carson PL, Scherzinger AL, Bland PH, Meyer CR, Schmitt RM, Chenevert TL, Bookstein FL, Bylski DI, Silver TM (1983) Advanced ultrasonic imaging for breast cancer diagnosis. In: Jellins J, Kobayashi T (eds) Ultrasonic Examination of the Breast, pp 187–199

Devaney A (1982a) Inversion formula for inverse scattering within the Born approximation. Opt Lett 7:111–112

Devaney A (1982b) A filtered backpropagation algorithm for diffraction tomography. Ultrason Imaging 4:336–350

Duric N, Littrup P, Babkin A, Chambers D, Azevedo S, Kalinin A, Pevzner R, Tokarev M, Holsapple E, Rama O, Duncan R (2005) Development of ultrasound tomography for breast imaging: technical assessment. Med Phys 32(5):1375–1386

Duric N, Littrup PJ, Rama O, Holsapple ET (2006) Computerized ultrasound risk evaluation CURE: first clinical results. Acoust Imaging 28:177–185

Duric N, Littrup P, Poulo L, Babkin A et al (2007) Detection of breast cancer with ultrasound tomography: first results with the computed ultrasound risk evaluation prototype. Med Phys 34(2):773–785

Glover GH (1977) Computerized time-of-flight ultrasonic tomography for breast examination. Ultrasound Med Biol 3(2–3):117–127

Glover G, Sharp J (1977) Reconstruction of ultrasound propagation speed distributions in soft tissue: time of flight tomography. IEEE Trans Sonics Ultrason SU-24:229–234

Greenleaf J, Bahn R (1981) Clinical imaging with transmissive ultrasonic computerized tomography. IEEE Trans Biomed Eng BME-28(2):231

Greenleaf J, Johnson S, Lee SL et al (1974) Algebraic reconstruction of spatial distributions of acoustic absorption in tissue from their two-dimensional acoustic projections. Acoust Holography 5:591–603

Greenleaf J, Johnson S, Samayoa W, Duck F (1975) Algebraic reconstruction of spatial distributions of acoustic absorption in tissue from their two-dimensional acoustic projections. Acoust Holography 6:71–90

Greenleaf JF, Johnson SA, Lent AH (1978) Measurement of spatial distribution of refractive index in tissues by ultrasonic computer assisted tomography. Ultrasound Med Biol 3(4):327–339

Hiller D, Ermert H (1980) Tomographic reconstruction of B-scan images. Acoust Imaging 10:347–364

Hong A, Rosen E, Soo M et al (2005) BI-RADS for sonography: Positive and negative predictive values of sonographic features. AJR 184(4):1260–1265

Howlader N, Noone AM, Krapcho M et al (eds) (2011) SEER cancer statistics review, 1975–2008. National Cancer Institute, Bethesda http://seer.cancer.gov/csr/1975_2008/, based on Nov 2010 SEER data submission, posted to the SEER web site

Johnson S, Abbott T, Bell R, Berggren M, Borup D et al (2007) Non-invasive breast tissue characterization using ultrasound speed and attenuation: in vivo validation. Acoust Imaging 28:147–154

Kaveh M, Mueller RK, Rylander R, Coulter TR, Soumekh M (1980) Experimental results in ultrasonic diffraction tomography. Acoust Imaging 9:433–450

Kelly KM, Dean J, Comulada WS, Lee S.-J. (2010) Breast cancer detection using automated whole breast ultrasound and mammography in radiographically dense breasts. Eur Radiol 20:734–742

Kolb T, Lichy J, Newhouse J (2002) Comparison of the performance of screening mammography, physical examination, and breast US and evaluation of factors that influence them: an analysis of 27,825 patient evaluations. Radiology 225:165–175

Kwak Y, Kim E, Park H et al (2006) Application of the breast imaging reporting and data system final assessment system in sonography of palpable breast lesions and reconsideration of the modified triple test. J Ultrasound Med 25(10):1255–1261

Mendelson EB, Baum JK, Berg WA, Merritt CB, Rubin E (2003) Breast imaging reporting and data system BI-RADS: ultrasound. In: D'Orsi CJ, Mendelson EB, Ikeda DM et al (eds) Breast imaging reporting and data system, 1st edn. American College of Radiology, Reston

Mueller RK, Kaveh M, Wade G (1979) Acoustical reconstructive tomography and applications to ultrasonics. Proc IEEE 67:567–586

Scherzinger AL, Belgam RA, Carson PL, Meyer CR et al (1989) Assessment of ultrasonic computed tomography in symptomatic breast patients by discriminant analysis. Ultrasound Med Biol 15:21–28

Shetty M, Shah Y, Sharman R (2003) Prospective evaluation of combined mammographic and sonographic assessment in patients with palpable abnormalities of the breast. J Ultrasound Med 22(3):263–268

Silverstein M, Lagios M, Recht A et al (2005) Image-detected breast cancer: state of the art diagnosis and treatment. J Amer Coll Surg 201(4):586–597

Stavros AT (2004) Breast ultrasound. Lippincott Williams & Wilkins, New York, pp 1–1015

Stavros A, Thickman D, Rapp C et al (1995) Solid breast nodules: use of sonography to distinguish between benign and malignant lesions. Radiology 196(1):123–134

Wiskin J, Borup D, Johnson S et al (2007) Full wave, non-linear, inverse scattering: high resolution quantitative breast tissue tomography. Acoust Imaging 28:183–194

Wiskin J, Borup D, Johnson S (2011a) Inverse scattering theory. Acoust Imaging 30:53–60

Wiskin J, Borup D, André M et al (2011b) Inverse scattering results. Acoust Imaging 30:61–68

Wiskin J, Borup D, Johnson S, Berggren M (2012) Nonlinear inverse scattering: high resolution quantitative breast tissue tomography. J Acoust Soc Am 131(5):3802–3813

Wolf E (1969) Three-dimensional structure determination of semi-transparent objects from holographic data. Opt Comm 1:153–156